HHS Public Access

Author manuscript

Sci Signal. Author manuscript; available in PMC 2024 July 04.

Published in final edited form as:

Sci Signal. 2023 July 04; 16(792): eabn8668. doi:10.1126/scisignal.abn8668.

Clustering of phosphatase RPTPα promotes Src signaling and the arthritogenic action of synovial fibroblasts

Sho Sendo[1,*], **William B. Kiosses**[1,2,*], **Shen Yang**[1], **Dennis J. Wu**[1], **Daniel W. K. Lee**[1], **Lin Liu**[1], **Yael Aschner**[4], **Allison J. Vela**[1], **Gregory P. Downey**[3,4,5,6,7], **Eugenio Santelli**[1], **Nunzio Bottini**[1,8]

[1]Dept. of Medicine, University of California San Diego, La Jolla, CA 92093

[2]La Jolla Institute for Immunology, La Jolla, CA 92037

[3]Division of Pulmonary, Critical Care, and Sleep Medicine, Department of Medicine, National Jewish Health, Denver, Colorado.

[4]Division of Pulmonary Sciences and Critical Care Medicine, Department of Medicine, University of Colorado, Aurora, Colorado.

[5]Department of Biomedical Research, National Jewish Health, Denver, Colorado.

[6]Department of Immunology and Microbiology, University of Colorado, Aurora, Colorado.

[7]Department of Pediatrics, National Jewish Health, Denver, Colorado.

[8]Department of Medicine, Kao Autoimmunity Institute, Cedars Sinai Medical Center, Los Angeles, CA, USA

Abstract

Receptor-type protein phosphatase α (RPTPα) promotes fibroblast-dependent arthritis and fibrosis in part by enhancing the activation of the kinase Src. Synovial fibroblasts lining joint tissue mediate inflammation and tissue damage, and their infiltration into adjacent tissues promotes disease progression. RPTPα includes an ectodomain and two intracellular catalytic domains (D1 and D2), and in cancer cells undergoes inhibitory homodimerization, which is dependent on a D1 wedge motif. Here through single-molecule localization and labeled molecule interaction microscopy of migrating synovial fibroblasts, we investigated the role of RPTPα dimerization in the activation of Src, the migration of synovial fibroblasts, and joint damage in a mouse model of

Address correspondence to: Nunzio Bottini, MD, PhD, T: 858-246-2398, nunzio.bottini@cshs.org.

*These authors contributed equally

AUTHOR CONTRIBUTIONS

S.S., W.B.K., D.J.W., D.W.K.L. and A.V. contributed to acquisition and analysis of data., L.L. led the statistical analysis, S.Y., G.P.D. and E.S. helped with design, performance and analysis of experiments., Y.A. and G.P.D. provided a critical reagent, S.S., W.B.K., D.J.W., and N.B. contributed to study conception and design. S.S., W.B.K. and N.B contributed to interpretation of data and wrote the manuscript. All authors reviewed and provided input on the final version of the manuscript.

COMPETING INTERESTS

NB is listed as an inventor on US patent 10,604,585 (assigned to the La Jolla Institute for Immunology) and on patent application PCT/US2022/074340 (assigned to the University of California San Diego) which are related to the findings of this study. NB has equity interests in Knoubis Bio, a company that may potentially benefit from the research results. The terms of this arrangement have been reviewed and approved by the University of California San Diego in accordance with its conflict of interest policies. The other authors have no known conflict of interest related to the studies described in this manuscript.

arthritis. RPTPα clustered with other RPTPα and with Src molecules in the context of actin-rich structures. A known dimerization-impairing mutation in the wedge motif (P210L/P211L) and the deletion of the D2 domain reduced RPTPα-RPTPα clustering, however it also unexpectedly reduced RPTPα-Src association. The same mutations also reduced recruitment of RPTPα to actin-rich structures and inhibited Src activation and cellular migration. An antibody against the RPTPα ectodomain that prevented the clustering of RPTPα also inhibited RPTPα-SRC association and Src activation and attenuated fibroblast migration and joint damage in arthritic mice. A catalytically-inactivating RPTPα-C469S mutation protected mice from arthritis, and reduced Src activation in synovial fibroblasts. We conclude that RPTPα clustering retains it to actin-rich structures to promote Src-mediated fibroblast migration and can be modulated through the extracellular domain.

INTRODUCTION

Protein Tyrosine Phosphatases (PTPs) promote or inhibit a multitude of signal transduction processes by counterbalancing the action of protein tyrosine kinases. The human genome encodes 22 putative transmembrane PTPs, classified in 8 subtypes(1). The R4 subtype receptor-type protein phosphatase α (RPTPα) is an example of a transmembrane PTP with two intracellular catalytic domains. The membrane-proximal domain, termed D1, is active in substrate dephosphorylation, while the membrane-distal domain called D2 displays very limited catalytic activity in vitro (2, 3) but is involved in functional regulation of the D1 domain(3–7).

A key function of RPTPα is to activate the SRC tyrosine kinase. RPTPα is known to be enriched in focal adhesions(8) (FA) and it is believed that the formation of a RPTPα-SRC complex is necessary to enable RPTPα-mediated dephosphorylation of SRC-Tyr^{527}(9, 10) which in turn promotes auto-phosphorylation of SRC on Tyr^{419}. The interaction between the SH2 domain of SRC and a phosphorylation Tyr^{789} (Tyr^{825} in the isoform used in this work) residue in the D2 domain of RPTPα reportedly promotes formation of such a complex(10) although it remains to be clarified whether this is the only mechanism(11). RPTPα is overexpressed in several cancers and is considered a therapeutic target to reduce activation of SRC and cancer cell growth(12, 13). RPTPα also plays an important role in the pathogenic action of fibroblast populations. In fibroblasts RPTPα -but not its Y789F mutant- is enriched in FA(8) and RPTPα deletion or Y789F mutation impairs FA function and cell migration through a pathway that involves Ras-related C3 botulinum toxin substrate 1 (RAC1) (14, 15). RPTPα enhances transforming growth factor β-mediated myofibroblast formation and collagen deposition and genetic deletion of RPTPα ameliorates disease severity in pre-clinical models of pulmonary fibrosis(16, 17). In inflammatory arthritis, RPTPα is highly expressed in a local joint-lining fibroblast population called synovial fibroblasts (SF) and promotes SF migration and pathogenic action (18). Accordingly, genetic deletion of RPTPα protects mice from arthritis in the SF-dependent K/BxN serum transfer induced arthritis (STIA) mouse model(18)

PTPs can be therapeutically targeted through allosteric inhibitors,(19–21) however a deep understanding of the regulation mechanisms of a PTP of interest is needed in order to design

appropriate targeting strategies. The isolated D1 domain of RPTPα can form a symmetric dimer through an interaction between a juxtamembrane wedge motif (encompassing aa 206–238) of one monomer and the active site of the other monomer(22). Another report shows that a disulfide-inducing P137C mutation of the transmembrane domain of RPTPα leads to reduced SRC activation in embryonic mouse cells, which could be rescued by a P210L/P211L mutation(23). Immunoprecipitation studies in HEK293 cells confirm the de-dimerizing effect of the P210L/P211L mutation and suggest that the D2 domain promotes while the extracellular domain (ECD) is dispensable for RPTPα dimerization(24).These reports and similar studies of other transmembrane PTPs(25, 26) point to dimerization through the wedge motif a potential shared mechanism of inhibition of transmembrane PTPs. However, (23) other structural and cellular studies suggest that regulation of RPTPs by the wedge motif depends on cellular contexts and/or might not apply to all RPTPs (7, 27–32). For example, RPTPα clusters can be detected by Förster Resonance Energy Transfer (FRET) microscopy in SK-N-MC neuroepithelial tumor cells expressing truncations of RPTPα in fusion with fluorescent proteins, however the wedge motif is dispensable for RPTPα clustering in these cells(33).

Here, in this manuscript, we revisited RPTPα dimerization by focusing on the migration of primary SF. We combined single molecule resolution (using the stochastic optical reconstruction microscopy -STORM- technique) and labeled molecule interaction (using FRET) microscopy methodologies with functional assays in SF expressing dimerization-impairing RPTPα mutants or treated with a de-clustering anti-RPTPα antibody. We also leveraged newly generated mice carrying a catalytically inactivating C469S mutation of RPTPα. Our data supported the idea that RPTPα undergoes substantial and wedge motif-dependent polarized clustering on the surface of migrating SF. However, they also suggested that in migrating fibroblasts RPTPα clustering promotes its recruitment to actin-rich structures and phosphatase activity-dependent activation of SRC.

RESULTS

Clustering of RPTPα and association of RPTPα with SRC occurs in actin-rich compartments of migrating SF

To begin to address the role of RPTPα dimerization on SRC signaling we focused on cytoskeletal actin projections of migrating SF by using total internal resolution microscopy (TIRF) and utilized single molecule resolution microscopy (using STORM) to accurately spatially localize RPTPα and SRC. SF from *PtpraP*TPRA-KO mouse (αKO SF) were transfected with plasmids expressing FLAG-tagged WT RPTPα or the dimerization-impairing P210L/P211L (P210) wedge mutant of RPTPα(23). Tagging of RPTPα did not affect its ability to co-precipitate with SRC (fig. S1). Monolayers of transfected SF were subjected to a scratch-wound assays followed by fixation and staining with Alex Fluor 647 (AF647) - conjugated anti-FLAG antibodies (Ab), AF568 conjugated anti-SRC Ab (Fig. 1a **left upper scheme**) and phalloidin fluorescein isothiocyanate (FITC) reagent (to stain F-actin) and cells were imaged by TIRF-STORM. Cells at the wound edge with a classical migrating phenotype characterized by protruding ruffles, filopodia and lamellipodia in the direction of the wound were captured using TIRF microscopy labelled for phalloidin (green

in Fig. 1a-I), RPTPα (red in Fig. 1a-I) and SRC (yellow in Fig. 1a-I), prior to STORM imaging. From STORM data, SRC-SRC, RPTPα-RPTPα and SRC-RPTPα co-localization maps(34) were constructed (Fig. 1a-II) where RPTPα or SRC fluorescent signals were represented as spheres. The sphere diameter represents the localization accuracy while the centroid is used to compare distances between same or different paired molecules (Fig. 1a-III). The RPTPα-SRC co-localization map was overlayed with TIRF images in order to define cellular polarity, and demonstrate the association of RPTPα, SRC and their clusters with polarized actin-rich structures, including basal stress fibers (BSTRESS), aligned in the direction of migration, and leading edge actin-rich structures (lamellipodia, ruffles and filopodia, LEDGE) (Fig. 1a **left lower scheme** and Fig. 1a-III-V).

We adopted 65 nm as the cut off distance separation to infer the closest realistic co-localization (pointing to in-cell molecule-molecule clustering or dimerization) between RPTPα and other RPTPα molecules (red spheres in Fig. 1a-III-V). This distance was inferred from molecular modeling of RPTPα dimers bound to their respective fluorophore-tagged Ab based on multiple crystal structures of RPTPα intracellular domain (7, 22) and a full-length mouse IgG1 antibody (1IGT)(35). Our model assumed that helices α1' and α2' from at least one of the D2 domains detach from the core PTP domain in order to allow dimerization of D1 and suggested a maximum theoretical distance between fluorophores of 55–70 nm, leading us to conclude that any distance >65 nm is unlikely due to RPTPα clustering/dimerization (fig. S2a-I). Structural information about RPTPα-SRC association is limited(36, 37), however similar modeling of the RPTPα-SRC association (fig. S2a-II) suggested a maximum theoretical distance between RPTPα and SRC fluorophores between 25 and 45 nm, thus we concluded that the >65 nm cutoff is also very likely to exclude functionally relevant colocalization while capturing all in-cell protein-protein interaction between SRC and RPTPα (white spheres in Fig. 1a-III,IV). Similarly, head to toe dimerization of SRC has been reported(38), which might be important to promote the activity of SRC and the phosphorylation of downstream effectors. While the structure of SRC dimers has not been resolved, modeling of SRC in complex with anti-SRC Ab (fig. S2b) suggests that the >65-nm cutoff is similarly very likely to exclude non-functionally relevant clustering between SRC and other SRC molecules (yellow spheres in Fig. 1a-III-V).

Our microscopy assessment showed that the LEDGE and BSTRESS areas were strongly enriched with clustered RPTPα-RPTPα (Fig. 1a-III-V, quantified in Fig. 1b) and SRC-SRC molecules (<65 nm, red and yellow spheres respectively). On the other hand, non-clustered RPTPα molecules (>65 nm) appeared to be randomly distributed across cellular compartments outside the actin rich labelled zones (blue spheres in Fig. 1a-V). We next analyzed clustering between RPTPα and SRC molecules. The association (<65 nm) between RPTPα molecules and SRC was also enriched in LEDGE and BSTRESS area (white spheres in Fig. 1a-III,IV and quantification in Fig. 1c). These results are consistent with the reported evidence that a considerable proportion of RPTPα molecules on the cell surface is dimerized and that RPTPα and presumably RPTPα-SRC complexes are enriched in FA (24, 33). However, the localization of RPTPα clusters to actin-rich structures, where also RPTPα-SRC and SRC-SRC clusters are enriched, is less consistent with the proposed inhibitory effect of dimerization on the function of RPTPα.

De-clustering mutations of RPTPα decrease its association with SRC in the LEDGE of migrating SF

We next compared, in the same TIRF-STORM assays, the phenotype of migrating αKO SF expressing WT- RPTPα or the known de-dimerizing P210L/P211L mutation of RPTPα (24) (Fig. 1d **left scheme**). Consistent with previous reports about the effect of the P210L/P211L mutation on RPTPα dimerization(23), co-localization of RPTPα was significantly reduced by the P210L/P211L mutation (representative TIRF alone in Fig. 1d-I,II, representative merged TIRF-STORM in Fig. 1d-III,IV, quantification in Fig. 1e). The mutation also mostly eliminated the enrichment of RPTPα clusters at LEDGE and BSTRESS (fig. S3a) and reduced the colocalization of RPTPα with SRC at LEDGE and BSTRESS (quantified in Fig. 1f and Fig. S3b,c) suggesting that RPTPα clustering might promote the recruitment or retention of RPTPα to SRC-enriched actin-rich structures of migrating SF and its association with SRC.

To further investigate RPTPα clustering and RPTPα-SRC association in migrating SF, we used multiple established FRET microscopy-based analytical methods using Ab labeled with donor (AF488) or acceptor (AF568) fluorophores (FRET pairs, Fig. 2a). These techniques are based on the occurrence of FRET when the donor and acceptor fluorophores are very close to each other (within 10 nm)(39). For technical reasons (see below) in these assays we mainly focused on LEDGE rather than BSTRESS.

FRET images of SF migrating at the edge of a scratch-wound (Fig. 2a-I) were processed based on previously established methods (40, 41) to show signal hot spots of molecule clustering. Each SF was separated into 4 compartments: leading edge, trailing edge and two lateral compartments (Fig. 2a-II,III) and the total area of FRET positive regions of interest (ROIs, Fig. 2a-IV, magnified in Fig. 2a-V) was automatically outlined. For the assessment of RPTPα clustering, αKO SF were transfected with plasmids expressing FLAG-tagged and HA-tagged WT RPTPα or its P210L/P211L (P210) mutant or a C-terminal deletion between at amino acids 560 and 818 that removes the D2 domain (dD2)(5), The latter construct includes the putative SRC-recruiting Tyr^{789}(10) residue. The cells were stained with AF488-labeled anti-HA Ab and indirectly AF568-labeled anti-FLAG Ab (Fig. 2a-**left upper scheme**). For the assessment of RPTPα-SRC association, αKO SF were transfected with plasmids expressing FLAG-tagged WT RPTPα or its P210L/P211L mutants or dD2 deletion and stained with AF488-labeled anti-SRC Ab and AF568-labeled anti-FLAG Ab (Fig. 2a-**left lower scheme**). As shown in Fig. 2b, c, HA-FLAG FRET occurred significantly at LEDGE of WT RPTPα-expressing cells (WT-WT); however, the P210L/P211L mutations (P210-P210 cells) and the dD2 deletion (dD2-dD2 cells) significantly reduced the area of FRET positive region at LEDGE. % SE FRET efficiency [calculated using the precise FRET (pFRET) method(42–44)] at LEDGE was also significantly reduced in P210-P210 and dD2-dD2 cells when compared to WT-WT cells (Fig. 2c). These data are in agreement with published literature and further consolidate the notion that the RPTPα P210L/P211L and dD2 mutations significantly reduce clustering of RPTPα at the LEDGE of a primary cell model. We next investigated the effect of the two mutations on RPTPα-SRC association using SEcFRET (Fig. 2d). The area of FRET signal and % FRET efficiency (using pFRET) in LEDGE was substantially reduced in cells expressing the P210L/P211L or the dD2

mutants of RPTPα (P210-SRC and dD2-SRC cells respectively) when compared to cells expressing WT RPTPα (WT-SRC cells) (Fig. 2e).

In order to circumvent some of the known shortcomings of SE FRET(39) we next applied spectral-based acceptor photobleaching FRET (apFRET) and fluorescence lifetime imaging FRET (FLIM-FRET) to the study of RPTPα clustering and RPTPα-SRC association in migrating SF. Spectral-based FRET(42) efficiently removes the contribution of donor spectral bleedthrough to the FRET signal. Only cells with truly FRET positive LEDGE at SEcFRET were selected (Fig. 3a-I). FRET efficiency using apFRET is assessed by measuring the difference between the quenched donor signal in the presence of the acceptor, and the dequenched donor signal after the acceptor has been bleached (42, 45, 46). Two ROIs were marked within each cell, one to bleach, another serving as an unbleached control, so that that each cell served as its own control (Fig. 3a-II-IV), and also an area devoid of cells was selected serving as a background control (fig. S4-I). For accurate detection of LEDGE fluorescence intensity, we defined the LEDGE region within each ROI through smaller subdivisions of the ROIs to stringently outline the cell lamellipodium and exclude non-cellular area (see example in fig. S4-II,III). The mean change in LEDGE fluorescence intensity (Fig. 3a-V) was used to calculate the % FRET efficiency (42, 45, 46). Experiments were performed on SF lines transfected with constructs to express WT RPTPα (WT-WT), the P210L/P211L mutant (P210-P210 cells) or the dD2 deletion (dD2-dD2 cells) (Fig. 3b). As shown in Fig. 3c, significantly higher anti-HA donor fluorescence recovery after acceptor photobleaching and consequent % RPTPα- RPTPα FRET efficiency were observed at LEDGE of WT RPTPα-expressing cells (WT-WT) than in SF expressing the P210L/P211L mutant (P210-P210 cells) or the dD2 deletion (dD2-dD2 cells). Fig. 3d, e shows that significantly higher anti-SRC donor fluorescence recovery after acceptor photobleaching and consequent % RPTPα-SRC FRET efficiency were observed at LEDGE of WT RPTPα-expressing cells (WT-SRC cells) than in SF expressing the P210L/P211L mutant (P210-SRC cells) or the dD2 deletion (dD2-SRC cells) mutants of RPTPα.

FLIM can be used to detect changes in donor lifetime that accompany energy transfer to the acceptor during FRET(47, 48). In the phasor representation, the analysis of FLIM data is done by observing the clustering of pixels values in specific regions of the phasor plot and localizing donor populations within FRET loops (47–49) (Fig. 3f). Unquenched donor residing in photobleached areas in FRET pair WT-RPTPα samples (yellow boxes in Fig. 3f-I,II) or donor alone samples (control in Fig. 3g) yielded a no FRET population (N-FRET, red pseudocolor in Fig. 3f-II, red circles in Fig. 3f-III and in Fig. 3g bottom panels) which was distinct from low and high FRET populations expressing quenched donor (L- and H-FRET, yellow and white areas and circles in Fig. 3f-II, Fig. 3f-III, and Fig. 3g). In these experiments, unquenched donor lifetimes were around t=2.4 ns while successfully quenched populations, exhibiting H-FRET, had lifetimes around 1.2 ns (Fig. 3f). Experiments were performed on SF lines transfected with constructs to express WT RPTPα (WT-WT), the P210L/P211L mutant (P210-P210 cells) or the dD2 deletion (dD2-dD2 cells). Consistent with the earlier described data obtained through STORM, SEcFRET and apFRET, the FLIM study (Fig. 3g) showed that % FRET efficiency of clustered RPTPα was significantly higher in WT-WT (H-FRET in Fig. 3g) compared to either P210-P210 or dD2-dD2 SF (L-FRET in Fig. 3g). Altogether, the data collected with various FRET-microscopy approaches are

consistent with the super-resolution microscopy data and suggest that RPTPα clustering significantly occurs at the LEDGE and correlates with the association between RPTPα and SRC in these structures.

Clustering-dependent recruitment of RPTPα to LEDGE facilitates SRC activation and actin fiber formation

Since association of RPTPα with SRC activates SRC and RPTPα is necessary for the correct functioning of FA in fibroblasts (8, 15), we next assessed the effect of clustering-impairing mutants of RPTPα on formation of the SRC-dependent actin-enriched LEDGE. Cortactin is a key substrate of SRC and a marker for polarized LEDGE formation (50, 51). Once phosphorylated, it is recruited to the actin cytoskeleton where it contributes to stress fiber stabilization (51). RPTPα is reportedly necessary for appropriate phosphorylation of cortactin in Caco-2 cells(52) Staining of migrating SF with anti-cortactin Ab showed that cortactin was less expressed in the LEDGE of SF expressing RPTPα clustering-impairing mutants, correlating with a reduced recruitment of RPTPα and SRC to the same region (Fig. 4a,b). Cortactin co-localized (using Manders overlap coefficients) with areas of RPTPα-SRC FRET (Fig. 4a) and RPTPα-cortactin and SRC-cortactin colocalization was also decreased in the LEDGE of SF expressing one or both clustering-impaired mutants of RPTPα (Fig. 4c and Fig. S5). Previous studies have suggested that SRC can promote RPTPα functions in cell migration in a positive feedback mechanism(14, 53). In line with those findings, inhibition of SRC activity, which reduced its recruitment to the actin cytoskeleton, also strongly reduced RPTPα-SRC co-localization (Fig. 4d,e). These results suggest a model in which SRC activation during migration facilitates RPTPα recruitment to and clustering at the LEDGE. Association of clustered RPTPα with SRC in turn leads to further activation of SRC, which promotes recruitment of cortactin and further formation of the LEDGE.

RPTPα clustering-deficient mutations behave as loss of function in migrating SF

Since SRC-dependent promotion of F-actin assembly is a key enabler of fibroblast migration and RPTPα is known to promote RAC activation in fibroblasts, the above-mentioned model predicts that clustering-deficient mutants of RPTPα inhibit activation of SRC and RAC and migration of SF. We tested this prediction by assessing SRC activation and migration in SF lines transfected with either empty vector or constructs to express WT RPTPα, the P210L/P211L or the dD2 deletion mutants (Fig. 5a). Consistent with our model, expression of WT RPTPα but not the P210L/P211L mutant or the dD2 deletion promoted migration of SF in two different assays (Fig. 5b-e). The same mutants failed to promote phosphorylation of SRC on Tyr^{419} and downstream phospho-RAC induction in migrating SF in microscopy assays of transfected cells. (Fig. 5f,g and fig. S6a,b).

RPTPα-blocking antibody (2F8) inhibits RPTPα clustering and association with SRC in migrating SF

To further support our model, we sought to acutely alter clustering of RPTPα through non-genetic interventions looking in parallel for FRET microscopy phenotypes and changes in SF migration assays. It remains an open question about whether RPTPα dimerization can be modulated through the extracellular domain. Thus, using αKO SF transfected with

plasmids expressing FLAG-tagged with or without HA-tagged WT RPTPα (named WT-WT and WT-SRC as in Fig. 2a), we first assessed the effect of a known monoclonal antibody (Ab) raised against the extracellular domain of RPTPα (clone 2F8, fig. S7a-c)(54) on the clustering of RPTPα and its association with SRC in migrating SF (Fig. 6a). Incubation of migrating WT-WT and WT-SRC SF with 2F8 Ab, but not with isotype control Ab or without 2F8 Ab, led to significant de-clustering of RPTPα (Fig. 6b,c, fig. S8a, S8b) in SEcFRET and apFRET assays, reduced association of RPTPα with SRC (Fig. 6d, fig. S8c) in SEcFRET assays and SRC activation in wound edge SF (Fig. 6e). Next, we assessed whether incubation with 2F8 Ab had any significant effect on unmanipulated SF migration. Incubation of SF with 2F8 Ab led to a significant reduction of migration of WT but not αKO SF in two independent assays (Fig. 6f,g and fig. S9a,b). When intra-articularly administered to mice with STIA -a model where SF migration is known to promote structural damage(55)- 2F8 also protected mice from cartilage damage and bone erosions (Fig. 6h,i). Thus, interfering with the extracellular domain of RPTPα with an Ab enables rapid de-clustering of endogenous RPTPα that correlates with a RPTPα loss of function phenotype in migrating SF.

RPTPα inactivation reduces arthritis severity in mice and removes the inhibitory effect of 2F8 Ab on SF migration

Next, we attempted to reconcile our observation that clustering of RPTPα promotes the phosphatase function in fibroblasts with the current wedge-mediated inactivation model of RPTPα dimerization. The vast majority of RPTPα phosphatase activity resides in the D1 domain with negligible contribution from the D2 (7). In order to assess whether the phosphatase activity of RPTPα contributes to its pro-inflammatory action in arthritis, we generated a knock-in mouse model carrying an inactivating C469S mutation of the catalytic Cys of the D1 domain (Fig. 7a). Homozygous RPTPα C469S (CS/CS) mice were born at Mendelian frequencies and displayed no clinically evident abnormalities or reduced lifespan or fertility. We then subjected CS/CS and littermate WT mice to STIA as in (18). Consistent with the phenotype of the RPTPα KO in the same model(18), C469S mutation of RPTPα protected mice from STIA although the phenotype was milder compared to the RPTPα KO(18) (Fig. 7b). We next generated SF lines from CS/CS mice and subjected them to migration assays in the presence of the 2F8 Ab and confirmed that the expression of RPTPα was similar between WT SF and CS/CS SF (Fig. 7c). The C469S mutation reduced SRC activation in migratory SF and removed the inhibitory effect of 2F8 Ab on SF migration in these cells (Fig. 7d and 7e). From these experiments, we conclude that activation of SRC following RPTPα clustering-dependent recruitment in SF is at least in part dependent on RPTPα phosphatase activity, as diagrammatically shown in (Fig.8) together with the rest of the model suggested by this study.

DISCUSSION

Several studies have addressed the potential effect of dimerization on the function of RPTPα and other transmembrane PTPs (22, 23). The role of the wedge motif in allosteric regulation of PTP activity has been supported by many but not all studies(7, 25–30, 32, 33, 56, 57). Our study addressed several gaps in the regulation of RPTPα by dimerization and how

RPTPα promotes the pathogenesis of inflammatory arthritis and likely also fibrosis by modulating SRC activation during fibroblasts migration (12, 13, 16–18). Our results also provide support for the therapeutic targeting of RPTPα through allosteric inhibition(19–21, 58–60).

SF are \ pivotal in the pathobiology of inflammatory arthritis leading to cartilage and bone damage that is observed in RA. Several reports correlate SF migration and invasion to promotion of arthritis severity in vivo(18, 61, 62). However, despite the growing importance of SF as players and potential therapeutic targets for RA, their mechanism of invasion remains incompletely understood and there is a paucity of studies focused on the dynamic aspects of migration of SF related to RA disease pathogenesis. Here, we have applied super-resolution TIRF-STORM and FRET approaches to unveil the molecular clustering of RPTPα and its recruitment mechanism at the leading edge of SF migration, combined with the study of RPTPα de-clustering mutations and Ab and of SF carrying a phosphatase-inactivating mutation of RPTPα. Our working model is depicted in Fig. 8. We found that SF migration leads to extensive enrichment of clustered RPTPα in actin-and cortactin-rich LEDGE and BSTRESS. The clustering of RPTPα and its enrichment at the LEDGE are promoted by SRC activation and inhibited by a known de-dimerizing RPTPα wedge mutation. Clustering of RPTPα strongly correlated with its association with SRC and further promoted SRC activation, formation of F-actin rich structures and cell migration.

The intracellular co-localization between SRC and RPTPα and the positive regulation of RPTPα recruitment to LEDGE by SRC were consistent with previous findings in the RPTPα literature. RPTPα is enriched in fibroblast actin-rich structures and also co-precipitates with SRC and other FA proteins(8, 10, 53). A complex between SRC and RPTPα exists based on an unbiased kinase-phosphatase interactome study(63). SRC-mediated positive regulation of RPTPα recruitment to FA which in turn promotes cell migration has also been reported (14) (53). The exact mechanism of SRC mediated recruitment of RPTPα to the LEDGE and how clustering of RPTPα contributes to this process remains to be clarified. However, it is tempting to speculate that phosphorylation of RPTPα-Tyr^{789} by SRC plays a role because this residue is a potential SRC phosphorylation site(64) and necessary for recruitment of RPTPα to FA and RPTPα-mediated promotion of cell migration(8, 14, 53). Given the enrichment of SRC-SRC clusters observed in actin-rich regions and since SRC dimerization is important to promote its downstream signaling (38), dimerization of SRC in actin-rich regions might also participate to the mechanism of RPTPα recruitment.

Our working model is consistent with the proposed role of the wedge motif in RPTPα dimerization. However, clustering-mediated promotion of RPTPα function needs to be reconciled with the “canonical model” of wedge-mediated inhibition of RPTPα, which postulates reciprocal occlusion of monomer active sites by wedge motifs(22). One explanation -supported by the milder phenotype induced by the C469S mutation compared to complete deletion of RPTPα - is that clustering promotes of RPTPα functions in part through activity-independent mechanisms. On the other hand, it is possible that, at least in migrating SF, the wedge motif promotes RPTPα dimerization and/or a different type of molecular clustering through a mechanism different from the canonical model. For

example, the wedge mutations can disrupt clustering in an indirect fashion by affecting the transmembrane domain of RPTPα, which was previously shown to be a more potent inducer of dimerization than the wedge motif(24).

In addition to wedge mutations, deletion of D2 also significantly reduced RPTPα clustering and RPTPα-SRC association and behaved as a loss of function mutant in migrating SF. These data were consistent with reports that the D2 domain is a potential interactor of the wedge domain(4) and promotes RPTPα dimerization and function (5, 6, 65).

The extensive clustering of RPTPα observed in SF was in agreement with another study showing dimerization of RPTPα in SK-N-MC cells(33), however the previous study could not detect strong inhibition of dimerization by the P210L/P211L mutation or the D2 deletion. Such discrepancy could be due to biochemical differences between transformed neuroepithelial cells and primary fibroblasts. However, the approaches used in the two studies are also different and each have their own limitations. Our study used tagged protein stained with Ab, whereas previous work relied on expression of truncations with fusion to fluorescent proteins (33). Unfortunately, despite testing multiple anti-RPTPα Ab, we could not find one that would provide sufficiently specific signal in fluorescence microscopy of mouse cells (when KO cells were used as controls) to enable the use of untagged protein. However, our assays using the 2F8 Ab on unmanipulated SF supported the idea that our findings on transfected αKO SF were representative of the regulation of endogenous RPTPα in SF.

Multiple lines of evidence in models of disease together with the finding that RPTPα KO mice have a benign phenotype, have validated RPTPα as a potential target for cancer, fibrosis and rheumatoid arthritis. We showed here that the role of RPTPα in arthritis is, at least in part, dependent on its phosphatase activity, suggesting that inhibitors of RPTPα D1 activity might have therapeutic relevance in arthritis. We also showed that RPTPα functions can be modulated by an Ab targeted to the extracellular domain with an inverse correlation between phosphatase clustering and inhibition of cell migration by the 2F8 Ab. Further studies of the 2F8 Ab as well application of our clustering assays to drug screening might help identify de-clustering biologic or small molecule agents with translational potential.

In conclusion, we have demonstrated compartmentalized and precise spatial intracellular localization of RPTPα clustering in a primary fibroblast subset where RPTPα is known to play an important role as a SRC activator. Our data lended further support to the role of PTPRA in FA and actin cytoskeleton organization in migrating cells. We also confirmed that the wedge motif plays a role in the regulation of RPTPα clustering and function. However, we suggest that the model of dimerization-induced phosphatase activity inhibition might need to be reconsidered, at least in certain physiological conditions. Since regulation of PTPs might vary depending on cell type, context and function considered, we believe that studies correlating protein clustering to function should be performed in the relevant cell types and contexts and before planning pharmacologic approaches to modulate transmembrane PTPs.

MATERIALS AND METHODS

Mouse models and STIA protocol

All mouse work was carried out in accordance to the Institutional Animal Care and Use Committee (IACUC) guidelines and approved by the UCSD IACUC (protocol #S16098). C57BL/6 and BALB/c mice were purchased from the Jackson Laboratory. RPTPα KO (αKO) mice on C57BL/6 background(54, 66) were generously shared by Drs. Jeroen den Hertog (Hubrecht Institute) and bred to obtain littermate WT or αKO mice. RPTPα C469S were generated using clustered regularly interspaced short palindromic repeats (CRISPR) knock-in approach at the National Taiwan University knockout mouse core. Heterozygous WT/CS mice were backcrossed onto the C57BL/6 background for 6 generations, then interbred to obtain littermate wild-type (WT) or CS/CS mice. KRN mice were a generous gift of Dr. Cristopher Benoist (Harvard University) and crossed with NOD mice to obtain offspring (K/BxN) that developed disease at around 6 to 7 weeks of age. Serum from arthritic K/BxN mice was pooled for use in the STIA model(18). To elicit STIA, 8–12 week-old mice were injected retro-orbitally with 200 μL of K/BxN serum. Arthritis was assessed by clinical scoring and measurement of ankles swelling every other day as described in (18), starting on the day of serum injection.

Intra-articular injection of 2F8 in STIA mice

Mice were randomized to two groups. K/BxN serum was intraperitoneally injected to BALB/c mice on day 0 and 2F8 Ab (40 μg/10 μL, N=9 mice) or phosphate buffered saline (PBS, N=10 mice) was intra-articularly injected in left hind paws of mice 3 days a week from day 0 to day 14. After mouse sacrifice on day 14, hind paws were fixed in 10% neutral buffered formalin, decalcified, and embedded in paraffin. Sections were prepared from the tissue blocks and stained with hematoxylin & eosin (H & E) and Toluidine blue (Inotiv). Histopathologic scoring was performed as previously described(67) in a blinded manner by two independent operators. The score of injected side was normalized by the score of the non-injected side to correct for mouse-to-mouse variability in arthritis severity and structural damage.

Antibodies

Mouse anti-FLAG antibody (F3165, AB_259529) was from Sigma Aldrich, rabbit anti-FLAG Alexa Fluor 647 conjugate antibody (3916S, AB_1658175), mouse anti-HA Alexa Fluor 488 conjugate antibody (2350S, AB_491023), rabbit anti-SRC antibody (2108S, AB_331137), rabbit anti-phospho-Rac1/cdc42 (Ser^{71}) antibody (2461S, AB_2300703) and rabbit anti-phospho-p44/42 MAPK (Erk1/2) (Thr^{202}/Tyr^{204}) antibody (4370S, AB_2315112) were from Cell Signaling Technology (CST), goat anti-mouse IgG Alexa Fluor 568 conjugate antibody (A11004, AB_2534072, A11031, AB_144696) and goat anti-rabbit IgG Alexa Fluor 488 conjugate antibody (A11008, AB_143165) and rabbit anti-phospho-SRC (Tyr^{419}) Alexa Fluor 488 conjugate antibody (44–660A1, AB_2533713) were from Invitrogen. Rabbit anti-cortactin Alexa Fluor 647 conjugate antibody (ab202650) and mouse anti-HA antibody (ab18181, AB_444303) were from Abcam. Rabbit anti-RPTPα Ab (13079–01-AP, AB_2269055) was from Proteintech. anti-Rabbit anti-SRC AF568 conjugate antibody was conjugated in-house from 100 μL (6.7 μg) of anti-SRC antibody

(Cell Signaling Technology, 2108, AB_331137) with CF™568 Dye (Biotium, 92275). Anti-mouse IgG, horseradish peroxidase (HRP)-conjugated Ab (from sheep) (NA931, AB_772210) and anti-rabbit IgG, HRP-conjugated Ab (from donkey) (NA934, AB_772206) were from Cytiva. Rabbit anti-Armenian hamster IgG, HRP-conjugated Ab (ab5745, AB_955407) were from Abcam. Isotype IgG from Armenian hamster (400902) were from BioLegend. The hamster mouse anti-RPTPα hybridoma #2F8 was generated by Dr. Matthew Thomas (Washington University) and generously provided by Dr. Jan Sap (University of Paris)(54).

Hybridoma culture and antibody purification from supernatants

The 2F8 hybridoma was cultured in Iscove's Modified Dulbecco's Medium (IMDM; gibco 12440–053) with 10% fetal bovine serum (FBS; Omega Scientific), 2mM L-glutamine, 2mM Sodium Pyruvate, 100 units/ml penicillin, 100 g/ml streptomycin and 50 μg/ml Gentamicin (Life Technologies) at 37°C in a humidified 5% CO_2 atmosphere. Cells were collected into 50 ml tubes and centrifuged, then resuspended with IMDM with 1% FBS and cultured for 7 days. The supernatant was collected and stocked until reaching more than 1000 ml. Two ml Protein G Sepharose (Cytiva 17–0618-01) was packed into a 20 ml column and the column was equilibrated and washed twice with 10 ml binding buffer (Thermo scientific 21001). The supernatant was added into the column and incubated for 24 hours at 4°C. The column was washed 4 times with 10 ml binding buffer, then 1 ml elution buffer (Thermo scientific 21004) was added to the column and incubated for 5 minutes at room temperature then the protein was eluted into 15 ml tubes with 0.2 ml neutralizing buffer (1 M Tris-HCl PH 9.0) The elution process was repeated at least 4 times. The concentration of Ab was measured using a NanoDrop One (Thermo scientific) and the Ab was assessed by protein gel staining and western blotting (Suppl Fig. 6).

Plasmids

All cloning and mutagenesis work was contracted out to GenScript. WT RPTPα (NM_008980.2), P201L/P211L RPTPα and Delta-D2 (560–818) RPTPα were cloned into the pcDNA3.1 (+) backbone between the AfIII and XhoI restriction sites in frame with or without either C-terminal FLAG or HA tags. As for GFP construct, GFP was cloned into the pmaxCloning™ Vector backbone.

Synovial fibroblasts (SF)/ HEK 293T cells culture and transfection

SF lines were isolated from knee and ankle joints of female 8-week old WT, RPTPα KO or RPTPα C469S mice as described(62). SF were cultured in Dulbecco's modified Eagle's medium (DMEM; Fisher Scientific 10–017) with 10% fetal bovine serum (FBS; Omega Scientific), 2mM L-glutamine, 100 units/ml penicillin, 100 g/ml streptomycin (Pen/St) and 50 μg/ml Gentamicin (Life Technologies) at 37°C in a humidified 5% CO_2 atmosphere. For all experiments, SF were used between passages 3 and 10, and subjected to overnight starvation in 0.1% FBS (serum-starvation medium) before functional assays. For microscopy experiments, fibronectin from bovine plasma in PBS was added to the wells of 24 well-plates and round coverslips were added a day before cell seeding. After removing the fibronectin from each well, 1×10^5 SF in 1 ml 10% FBS DMEM were seeded in each well. Transfection with each plasmid (0.77 μg/well) was performed using Lipofectamine

3000 (Invitrogen L3000015) in DMEM with no additional additives once monolayer reached approximately 90% confluency. The transfection media was replaced with normal SF media (10% FBS DMEM) 3 hours after transfection. For assays, 36 or 48 hours after transfection, SF were starved for 12 hours in 0.1% FBS DMEM. HEK 293T cells (ATCC CRL1573) (1.5×10^5) were seeded in each well of a 6 well-plate 1 day before transfection. Plasmids encoding WT PTPRA-HA or untagged PTPRA (3 μg/well) was incubated with 9 μg of linear polyethylenimine (PEI) in 100 μL Opti-MEM (Gibco) for 15 min. The DNA/PEI admixture was added to the HEK 293T cells in 500 μl Opti-MEM and followed by addition of 2 ml of 10% FBS HEK 293T medium (DMEM with 10% FBS, 5% Pen/St, 5% HEPES, and 5% sodium pyruvate) and incubation for 48 hours.

Molecular modeling of RPTPα dimers and RPTPα-SRC complexes

The RPTPα dimer model was assembled using the structures of a RPTPα D2 dimer (pdb code 1YFO)(22), RPTPα D1 + D2 (6UZT)(7) and a full-length mouse IgG1 antibody (1IGT)(35) with simple manual re-building and geometry regularization of RPTPα D2 using coot(68). The RPTPα-SRC complex model was assembled using the structures of non-Tyr^{527}-phosphorylated SRC (pdb code 1Y57) (37), SRC SH2 bound to a RPTPα phosphopeptide (1P13) (36) and a full-length mouse IgG1 antibody (1IGT)(35) with simple manual re-building and geometry regularization of RPTPα D2 using coot(68).

Immunofluorescence Staining

Transfected SF layered on round coverslips were fixed with 4% paraformaldehyde (PFA) for 20 minutes and washed 3 times with PBS. The cells were permeabilized for 10 minutes with 1% bovine serum albumin (BSA), 0.2% TritonX-100 in PBS and washed 3 times with PBS containing 0.0001% TritonX-100. Samples were blocked with 2% BSA or 2% normal goat serum (life technologies, PCN5000) blocking buffer for 1 hour, incubated with primary Ab for 2 hours and then incubated with fluorescence-conjugated secondary Ab for 1 hour. In some experiments, samples were incubated with anti-cortactin AF648 Ab for 2 hours. For super resolution microscopy experiments, samples were stained with Phalloidin FITC reagent (Abcam ab235137) for 20 minutes. For staining with phospho-SRC, phospho-RAC and phospho-ERK Ab, samples were stained with AF647 Phalloidin (Invitrogen A22287) for two hours. All samples were stained with Hoechst 33342 (Life technologies H3570) for 10 minutes, washed twice with PBS containing 0.0001% TritonX-100. Then the coverslips were mounted onto glass slides.

Nikon N-STORM and TIRF Imaging and Imaris Analysis

RPTPα KO mouse SF were directly plated onto μ-Slide 8 Well (Ibidi) coverslips and allowed to grow to confluence in a 24 well plate. Cells were transfected once they had reached 90% confluency and starved for 12 h 36 h post transfection as described above. After starvation, a scratch wound was induced as described above. The wound was allowed to close for 12 h in high serum media (20% FBS) before cell fixation with 4% PFA. The cells were then permeabilized by 0.2% triton-X and stained with AF647 conjugate anti-FLAG Ab, AF568 conjugate anti-SRC Ab and phalloidin FITC reagent (for F-actin). The coverslips were then mounted onto slides with molecular probe gold reagent. As outlined in (34), cells were imaged using 100x (1.49 NA) Apo TIRF objective with TIRF illumination

on a Nikon Ti super-resolution microscope. Images were collected on an ANDOR IXON3 Ultra DU897 Electron Multiplying Charge Coupled Device (EMCCD) camera using the multicolor sequential mode setting in the NIS-Elements AR software (Nikon Instruments Inc., NY). The power on the 488, 561 and 647 nm lasers was adjusted to 50% to enable collection of between 100 and 300 molecules per 256 × 256 camera pixel frame in the center of the field at appropriate threshold settings for each channel. Collection was set to 20,000 frames, yielding 1–2 million molecules, and the super-resolution images were reconstructed with the Nikon STORM software. The position of individual molecules was localized with high accuracy by switching them on and off sequentially using the 488, 561 and 647 nm lasers at appropriate power settings. The position determined from multiple switching cycles can show a substantial drift over the duration of the acquisition. This error was reduced by correcting for sample drift over the course of the experiment by an auto-correlation method based on by correlating STORM images reconstructed from 200–1000 frames to that from the beginning of the acquisition(69). The number of frames used in a set was based on the number of molecules identified, and by default it was set to 10000 molecules. Displacement was corrected by translational displacement in the X, Y direction for 2D STORM. Axial drift over the course of the acquisition was minimized by engaging the Nikon perfect focus system. Calibration of chromatic shift (warp correction) was carried out using multicolored 100 nm TetraSpeck beads using minimum density per field of over 100 beads and using the 2D warp calibration feature of the Nikon STORM software. Briefly, a total of 201 images were collected for each of the color channels (488, 561 and 647 nm) paired with phalloidin for F-actin (AF488), SRC (AF568) and RPTPα (AF647) respectively, without the cylindrical lens in place. Frames 1–20 and frames 182–201 were collected at the focal position. Frames 21–181 were collected across a range of 1.6 μm in 10 nm steps in the Z (covering 800 nm above and 800 nm below the focal plane). The calibration files generated from this macro (software feature) were applied during analysis for the correction of the STORM images. All fixed and stained samples were incubated in the following blinking solution (STORM buffer(69): 50 mM Tris, pH 8.0, 10 mM NaCl, 10% glucose, 0.1 M mercaptoethanolamine (MEA), 56 units/ml glucose oxidase, and 340 units/ml catalase. The STORM buffer was prepared by adding 100 μL MEA solution and 10 μL GLOX sample (14 mg glucose oxidase [from *Aspergillus niger*-type VII, Sigma-Aldrich Cat # G2133] and 1 mg catalase [from bovine liver, Sigma-Aldrich Cat # C40] dissolved in 250 μL of 10 mM Tris, 50 mM NaCl pH 8.0) to 890 μL of buffer B (50 mM Tris, 10 mM NaCl, 10% Glucose, pH 8.0) just before imaging.

Blinking events were followed for successive frames to ensure single molecule isolation by filtering out molecules with traces longer than 5 frames during analysis. Moreover, individual molecules were localized using point spread function (PSF) width filters of 200–400 nm based on a 100x (1.49 NA) objective and restrictions were placed on photon count signals associated with camera noise of the ANDOR electron multiplying charge-coupled device (EM-CCD) camera (estimated at 100 intensity units above 0). The data was further filtered based on empirical observation of photon count signals (peak height when converted to an intensity value) found in cells vs background staining on the glass slide surface (generally values above 300–700 intensity units above camera noise). The precision of the

localization during a switching cycle is calculated from these multiple parameters and from photon counts using molecules that are ultimately well separated in the sample itself(70).

TIRF microscopy experiments were performed on the same multi-adapted N-STORM system using a 100x (1.45 NA) TIRF objective (Nikon Instruments, Melville, NY) on a Nikon TE2000U microscope custom modified with a TIRF illumination module as described(69). Images were acquired on a 14-bit, cooled charge-coupled device (CCD) camera (Hamamatsu) controlled through NIS-Elements software. After placing the cells on the stage, the position of the individual laser beams was adjusted with the TIRF illuminator to impinge on the coverslip at an angle to yield a calculated evanescent field depth of a 70–100 nm for TIRF microscopy modes, staying as close to the lamellipodia to glass surface as possible and maintained for subsequent N-STORM data collection. Cells only at the wound edge with a distinct and characteristic classical migrating phenotype with a ruffling and protruding lamellipodia in the direction of the wound were captured for phalloidin (green), RPTPα (far red) and SRC (yellow), prior to N-STORM imaging to be used in image processing as references of large biological compartments, like basal stress fibers, ruffles and leading edges.

Images obtained on the N-STORM system were exported as pointillism or localization coordinate map text files, which represent positions of individual blinks that have been localized with high accuracy by switching them on and off using the 488, 561 and 647nm lasers. The localization coordinates were imported into the Imaris software (Bitplane, Inc.) where each blink was reconstructed as a sphere (spot) on an image grid, its centroid is the central coordinate position in three-dimensional space, and the diameter of the sphere (spot) is the localization accuracy error. The widefield TIRF images were also imported into Imaris as separate channels, aligned and fitted to overlay with the N-STORM image. This is used to define cellular polarity, compartments and structures using the lesser resolved original fluorescent signals. Once imported into Imaris all spots were filtered for a minimum localization accuracy (diameter 0–100 nm) and whether they, between the same population (RPTPα or SRC) are clustered in pairs of 3, 6 or 9 molecules to filter single or lone stray molecules. However, all localizations are considered in calculations to ensure consistency between experiments. Furthermore, all spots created were analyzed using the colocalized spots module in Imaris, to mark and score paired spots between separately labelled populations of RPTPα to RPTPα or RPTPα to SRC that lie within a defined distance from each other in three-dimensional space based on their centroid.

Fluorescent (or Förster) Resonance Energy Transfer (FRET) methods

Cells were plated, transfected and fixed as described above, followed by staining with primary, secondary, and direct conjugate antibodies. We focused our FRET studies on LEDGE because the growing lamellipodial edge has a limited depth around the cell periphery at approximately 110–160 nm. (71–73). Moving inward from the cell edge to the nucleus, where BSTRESS are enriched on different cell planes the cell thickness in SF cells increases considerably (depending on the cell up to 2000nm or more). The confocal FRET and FLIM imaging equipment available to us enables enhanced resolution (120–140nm) on the x-y but not the z plane thus was only suited to robust assessment of the LEDGE.

SEcFRET and pFRET.—All images were acquired with a Zeiss laser scanning confocal microscope (LSM) 880 Airyscan using a 63x (1.46 NA) and a 63x (1.4 NA) objective using the 32-channel GaAsP-PMT area detector. In the Zen software, the capture method was designed to sequentially capture the donor channel [488 excitation, and emission 508–535 (27 lambda)], raw FRET channel [488 excitation and emission 588–624] and acceptor channel [568 excitation and emission 588–624)]. All 12-bit images were acquired with Nyquist resolution parameters using optimal pinhole sizes (pixel size 0.060×0.060 microns) and optimal frame size of 2644×2644. All 12-bit images were acquired using the full dynamic intensity range (0–4096) that was determined with the population of WT cells having the moderate to brightest signal expression of RPTPα and or SRC. For cFRET imaging, the system consisted of a 45-mW argon laser (458, 488, 514 nm), a 10-mW diode solid state laser (561 nm) and a He-Ne 633-nm laser. System settings were set as constants and defined based on the WT constructs: 1% laser power for acceptor, and 3% for both raw FRET channel and donor channels, detector signal amplification (digital gain) was set to 900V for all acquisitions, donor, raw FRET and acceptor. Both donor-acceptor samples and donor alone as well as acceptor alone controls were captured for every experiment and three images were obtained -namely: image 1: donor excitation to donor emission; image 2: acceptor excitation to acceptor emission; image 3: donor excitation to acceptor emission- in order to later incorporate background subtraction and spectral bleed through correction factors into the raw FRET samples using established automated algorithm methods of analysis. Algorithms to remove spectral bleedthrough/cross-talk and correct for spectral variations in donor and acceptor channels, autofluorescence, background fluorescence, detector and optical noise are all established components of cFRET methodologies. Using imageJ, we have automated and scripted our cFRET method developed earlier in both widefield and confocal platforms(74) (40, 41, 75). In addition, all images were also processed in order to calculate FRET efficiencies of all cells at the leading edge using the method of pFRET that was developed and scripted by Amassi Periasamy's group and incorporated into a complete data processing software package of ImageJ plugins written in JAVA(42–44, 76).

Cells for FRET analysis were selected among the ones expressing relatively equal expression (intensity range 700–4095) of FLAG and HA based on their overall average acquisition mean fluorescence intensities. All acquisition settings, including laser power, detector gain and laser scan speed and averaging (pixel dwell time 1.26 μs), were the same for all variants and experiments.

Final processed cFRET Images were further analyzed in Image Pro Premier 10 (IPP10) to define area and polarity of FRET positive regions of interest (ROIs) at the leading edge cell periphery. In order to automate and define distinct and broad FRET positive zone groupings for this assay, as was previously done(40, 41), images were converted to 8-bit greyscale and the FRET positive zones were auto-outlined using Image Pro Premier software tools (wand). Using this technique, the dynamic range of relevant FRET positive signal (compared between FRET methods) was between 85–256 for all samples and was used to outline FRET positive regions of interest (ROIs) that were scored for each quadrant and charted in excel. The same original raw data was also further processed in the pFRET software and % FRET

efficiencies were obtained for each cFRET sample post-processed for FRET positive zone area analysis.

apFRET.—All images were acquired with a Zeiss LSM 880 Airyscan using a 63x (1.46 NA) / or a 63x (1.4 NA) objective and the 32-channel GaAsP photomultiplier tubes (PMT) area detector. Using the spectral detector, as outlined in (42), donor alone and acceptor alone samples are acquired using the 32 channel spectral detector to establish emission curves that are then incorporated into the inherent on-line fingerprinting mode to auto correct for spectral bleedthrough The LSM 880 is designed with acousto-optic tunable filters that can be used to obtain images at a series of discrete 10 nm wavelength bands, generating lambda stacks. The spectral signatures for the individual 488 and 568 fluorophores and background signals are obtained from these lambda stacks and linearly unmixing is employed within the Zen software, to segregate mixed (overlapping) fluorescent signals to obtain the spatial contribution for each fluorophore known as emission online fingerprinting.

FRET efficiency using apFRET was calculated by measuring the difference between the quenched donor signal in the presence of the acceptor, and the dequenched donor signal after the acceptor has been bleached(42, 45, 46, 77, 78). FRET efficiency is defined over a time regimen of 30 cycles (roughly 300s) post bleaching, after 4 unbleached scans are acquired to establish a stable baseline stable fluorescence at each ROI selected. The Software module in Zen automatically tracks the mean changes in fluorescence intensity within the ROIs and is thus used to calculate the % FRET efficiency as outlined previously by others. Briefly, this is mathematically based on the % of donor fluorescence recovered between t=0 (the average of 4 unbleached scans) and the plateau peak of donor fluorescent recovery at approximately t=15m later(42, 45, 46, 77, 78). Regions far away from the leading edge that may dilute the overall FRET efficiency at the leading edge are omitted.

FLIM-FRET.—All the time-domain FLIM images were acquired with a Leica time-correlated single photon counting (TCSPC) SP8X Fast Lifetime Contrast (FALCON) system from Leica Microsystems (Mannheim, Germany). This integrated Time-Correlated Single Photon Counting Fluorescent Lifetime Imaging (TCSPC-FLIM) system utilizes a confocal scan head with field-programmable gated array (FPGA) electronics, pulsed laser excitation and fast, spectral single-photon counting detectors. The signals of both laser pulses and photon arrival pulses from each detector are digitized at very high speed with a temporal resolution of 97 ps. These direct measurements from the differences in arrival times between detection and excitation pulses are rendered directly online as ‘fast FLIM’ images, in a time resolved manner.

Donor alone was imaged from SF labeled with anti-HA (AF488) (Control) while donor and acceptor were imaged from SF labeled with anti-HA (AF488) and anti-FLAG (AF568) (FRET pair). Prolonged gold mounted samples were imaged under a 100x (1.4 NA) oil immersion objective. Donor excitation was achieved using a white light pulsed laser (laser power at 50%, 1.5–2 mW per line) tuned at 40 MHz coupled with single photon counting electronics and subsequently detected by highly sensitive hybrid internal detectors in photon counting mode. Collection parameters included: acquiring 8-bit (all converted internally to 16-bit final image) images pixel by pixel (512 × 512 frame size) with an emission collection

detection range of 498–584 nm, a detector gain set at 100 and scan speed at 400 Hz. Frame acquisitions averaging was 100 to accumulate enough photons at the cell periphery and at lamellipodia ruffling edges. As described in detail in (79, 80), to remove artefacts caused by noise or photo–bleaching and insufficient signal to noise, cells with negligible amounts of bleaching and at least 200–1000 photons per pixel were only allowed in the analysis. The acquired fluorescence decay of each pixel was deconvoluted with the instrument response function (IRF) and then post processed by being fitted with two-exponential theoretical models using Leica Application Suite X (LAS X) from Leica Microsystems. Using the Leica Applications suite, 2D phasor plot analysis loops were used to segregate single donor populations from FLIM-FRET populations(47, 49, 81).

Manders Overlap Coefficient Analysis

Correlation coefficients for spatial overlap were generated using the Zen Pro (Zeiss) and/or IPP10 (media Cybernetics) software colocalization modules. Briefly as described in detail in(82), cells was auto-outlined and thresholds of real signal above autofluorescence and background signals were defined by secondary antibodies alone on separate samples. For all 12 bit images obtained at Nyquist resolution (frame size 2644×2644), previously defined minimum fluorescent thresholds were input into Zen or IPP10, two fluorescent channels signals are selected and the software automatically calculates pixel intensity spatial overlap coefficients between them (both Manders and Pearsons are scored).

SRC inhibitor treatment

The SRC inhibitor SU6656 (S7774) was purchased from Selleckchem.com. After the scratch-wound, αKO SF transfected a plasmid encoding WT PTPRA-HA were cultured in 20% FBS DMEM for 12 hours and incubated with 5 μM of SU6656 or Dimethyl sulfoxide (DMSO) for additional 30 minutes, and then fixed with 4% PFA.

Transwell Migration Assay

Confluent SF after transfection were harvested by light trypsin digestion and seeded at 1–2.5 × 10^4 cells in 100 μL serum-free DMEM containing 0.5% BSA in the upper chamber of a 6.5 mm-diameter Transwell polycarbonate culture insert (Costar) with a pore size of 8 microns. Inserts were placed in 24-well plates with 600 μL DMEM containing 5% FBS. The assay plates were incubated for 4 h, after which the Transwell inserts were removed and the upper chamber gently wiped with a cotton swab to remove non-migrating cells. Transwell membranes were fixed for 10 min in prechilled (−80 °C) methanol and stained for 10 min in 0.5% crystal violet in 25% methanol. Cells were then rinsed and imaged using a Motic AE2000 microscope at 10x magnification. Cell migration was quantified by counting 4 random fields.

Wound Healing Assay

αKO SF were plated into 6 well plates and allowed to grow to 90% confluency before transfection as described above. 36 h post transfection cells were starved for 12 h, and a scratch wound was induced by drawing a micropipette tip through the middle of the coverslip. Pictures of the wound were acquired and the distance between the scratch margins

marked to constitute the 0h timepoint. The wound was allowed to heal for 24 h in high serum (20% FBS) media before acquiring another set of pictures of the same wound for the 24 h timepoint. Slides were then fixed and stained with crystal violet as described above and cells were visualized using a Motic AE2000 microscope at 4x magnification. Each scratch wound was scored at four separate locations by ImageJ distance quantification.

SF treatment with 2F8 Ab

For FRET microscopy experiments, 500 nM Ab isolated from 2F8 hybridoma supernatant in 1% FBS DMEM were added into the wells after removing 20% FBS DMEM and incubate for two hours before fixation. As a control, isotype IgG from Armenian hamster (BioLegend 400902) or no Ab were used. For transwell migration assay and wound healing assay, 500–1000 nM Ab were added 24 hours before analysis.

Quantitative real-time polymerase chain reaction (RT-qPCR)

Total RNA was extracted by RNeasy Plus Mini Kit (Qiagen 74136) according to the manufacturer's protocol. Mouse primers were obtained from Qiagen: RPTPα (PPM34001A) and *GapdhGAPDH* (PPM02946E). RT-qPCR was performed on complementary DNA synthesized with 2720 Thermal Cycler (Applied Biosystems) and evaluated on the Bio-Rad CFX384 Real-Time System. Reactions were measured in duplicate, and data were normalized to the expression levels of the housekeeping gene *GapdhGAPDH*.

Western Blotting (WB) and Protein Gel Staining

Cells were lysed in radioimmunoprecipitation assay (RIPA) buffer (Cell Signaling Technology 9806S) containing protease and phosphatase inhibitor (ThermoFisher A32961) and lysates were sonicated and centrifuged (13,200 rpm at 4°C for 20 min). The samples were resuspended in Sodium dodecyl-sulfate (SDS) denaturing buffer (1x Laemmli sample buffer, 5% beta mercaptoethanol, 2.05% SDS), and loaded onto SDS- polyacrylamide gel electrophoresis gels. The separated proteins in the gel were transferred onto nitrocellulose membranes at 40 volts at 60°C for 1.5 h. The membrane was blocked with 5% non-fat milk in Tris buffered saline solution for 1 hour. Primary Ab were diluted 1:1000 and incubated overnight, and secondary ab were diluted 1:3000 or 1:5000 and incubated for one hour. Luminescence detection was performed by ECL (Immobilon Crescendo Western HRP Substrate, MILLPORE WBLUR0500), on a Syngene image analyser (G:BOX). For protein gel staining, protein-containing SDS-PAGE gels were stained with Coomassie Protein Assay Reagent (Thermo scientific 1856209).

Co-immunoprecipitation

HEK 293T cells transfected with plasmids encoding WT PTPRA-HA or untagged PTPRA were lysed in RIPA buffer to get the lysate. Lysates were subjected to Immunoprecipitation (IP) performed with anti-SRC Ab and followed by Western blotting with anti-RPTPα Ab. 20 μL of the lysate was used as an input control.

Statistical analysis

All statistical analyses were performed using GraphPad Prism 9 software. Normality of data distribution was assessed using the Shapiro-Wilk test. Statistical comparisons between 2 groups were performed using Mann-Whitney or the t-test. For multiple comparisons, the Kruskal-Wallis test followed by corrected Dunn's test was used except for comparisons of spectral FRET data (normally distributed data) where ordinary one-way ANOVA followed by Dunnett's multiple comparison test calculated on the area under curve (AUC) was used. For FRET comparisons between two groups we utilized t-test. P values less than 0.05 were considered significant.

Supplementary Material

Refer to Web version on PubMed Central for supplementary material.

ACKNOWLEDGMENTS

We wish to thank Dr. Kersi Pestonjamasp, Dr. Ke Wang, and Ms. Megan Lee for expert technical assistance.

FUNDING

This study was supported by NIH grant AR066053 and a grant from Roche (to N.B.). D.J.W. was supported by NIH Training Grant T32 AR064194. We wish to acknowledge support from the NIAMS MARC Center at UCSD through grant P30AR073761 and grant S10OD021831 to La Jolla Institute for Immunology Imaging core facility.

DATA AND MATERIALS AVAILABILITY

All data supporting the findings of this study are found within the paper and its Supplementary Information. The original data related to the findings of this study are available from the corresponding author upon reasonable request.

REFERENCES

1. Alonso A et al. , Protein tyrosine phosphatases in the human genome. Cell 117, 699–711 (2004). [PubMed: 15186772]
2. Wang Y, Pallen CJ, The receptor-like protein tyrosine phosphatase HPTP alpha has two active catalytic domains with distinct substrate specificities. EMBO J 10, 3231–3237 (1991). [PubMed: 1915292]
3. Lim KL, Lai DS, Kalousek MB, Wang Y, Pallen CJ, Kinetic analysis of two closely related receptor-like protein-tyrosine-phosphatases, PTP alpha and PTP epsilon. Eur J Biochem 245, 693–700 (1997). [PubMed: 9183007]
4. Blanchetot C, den Hertog J, Multiple interactions between receptor protein-tyrosine phosphatase (RPTP) alpha and membrane-distal protein-tyrosine phosphatase domains of various RPTPs. J Biol Chem 275, 12446–12452 (2000).
5. Blanchetot C, Tertoolen LG, den Hertog J, Regulation of receptor protein-tyrosine phosphatase alpha by oxidative stress. EMBO J 21, 493–503 (2002). [PubMed: 11847098]
6. Yang J et al. , Reversible oxidation of the membrane distal domain of receptor PTPalpha is mediated by a cyclic sulfenamide. Biochemistry 46, 709–719 (2007). [PubMed: 17223692]
7. Wen Y et al. , RPTPalpha phosphatase activity is allosterically regulated by the membrane-distal catalytic domain. J Biol Chem 295, 4923–4936 (2020). [PubMed: 32139509]
8. Lammers R, Lerch MM, Ullrich A, The carboxyl-terminal tyrosine residue of protein-tyrosine phosphatase alpha mediates association with focal adhesion plaques. J Biol Chem 275, 3391–3396 (2000). [PubMed: 10652331]

9. den Hertog J et al. , Receptor protein tyrosine phosphatase alpha activates pp60c-src and is involved in neuronal differentiation. EMBO J 12, 3789–3798 (1993). [PubMed: 7691597]
10. Zheng XM, Resnick RJ, Shalloway D, A phosphotyrosine displacement mechanism for activation of Src by PTPalpha. EMBO J 19, 964–978 (2000). [PubMed: 10698938]
11. Vacaru AM, den Hertog J, Serine dephosphorylation of receptor protein tyrosine phosphatase alpha in mitosis induces Src binding and activation. Mol Cell Biol 30, 2850–2861 (2010). [PubMed: 20385765]
12. Elson A, Stepping out of the shadows: Oncogenic and tumor-promoting protein tyrosine phosphatases. Int J Biochem Cell Biol 96, 135–147 (2018). [PubMed: 28941747]
13. Lin C, Xin S, Huang X, Zhang F, PTPRA facilitates cancer growth and migration via the TNF-alpha-mediated PTPRA-NF-kappaB pathway in MCF-7 breast cancer cells. Oncol Lett 20, 131 (2020). [PubMed: 32934700]
14. Chen M, Chen SC, Pallen CJ, Integrin-induced tyrosine phosphorylation of protein-tyrosine phosphatase-alpha is required for cytoskeletal reorganization and cell migration. J Biol Chem 281, 11972–11980 (2006).
15. Herrera Abreu MT et al. , Tyrosine phosphatase PTPalpha regulates focal adhesion remodeling through Rac1 activation. Am J Physiol Cell Physiol 294, C931–944 (2008). [PubMed: 18216165]
16. Aschner Y et al. , Protein tyrosine phosphatase alpha mediates profibrotic signaling in lung fibroblasts through TGF-beta responsiveness. Am J Pathol 184, 1489–1502 (2014). [PubMed: 24650563]
17. Aschner Y et al. , Protein tyrosine phosphatase-alpha amplifies transforming growth factor-beta-dependent profibrotic signaling in lung fibroblasts. Am J Physiol Lung Cell Mol Physiol 319, L294–L311 (2020). [PubMed: 32491951]
18. Stanford SM et al. , Receptor Protein Tyrosine Phosphatase alpha-Mediated Enhancement of Rheumatoid Synovial Fibroblast Signaling and Promotion of Arthritis in Mice. Arthritis Rheumatol 68, 359–369 (2016). [PubMed: 26414708]
19. Krishnan N et al. , Targeting the disordered C terminus of PTP1B with an allosteric inhibitor. Nat Chem Biol 10, 558–566 (2014). [PubMed: 24845231]
20. Chen YN et al. , Allosteric inhibition of SHP2 phosphatase inhibits cancers driven by receptor tyrosine kinases. Nature 535, 148–152 (2016). [PubMed: 27362227]
21. Stanford SM, Bottini N, Targeting Tyrosine Phosphatases: Time to End the Stigma. Trends Pharmacol Sci 38, 524–540 (2017). [PubMed: 28412041]
22. Bilwes AM, den Hertog J, Hunter T, Noel JP, Structural basis for inhibition of receptor protein-tyrosine phosphatase-alpha by dimerization. Nature 382, 555–559 (1996). [PubMed: 8700232]
23. Jiang G et al. , Dimerization inhibits the activity of receptor-like protein-tyrosine phosphatase-alpha. Nature 401, 606–610 (1999). [PubMed: 10524630]
24. Jiang G, den Hertog J, Hunter T, Receptor-like protein tyrosine phosphatase alpha homodimerizes on the cell surface. Mol Cell Biol 20, 5917–5929 (2000). [PubMed: 10913175]
25. Majeti R, Bilwes AM, Noel JP, Hunter T, Weiss A, Dimerization-induced inhibition of receptor protein tyrosine phosphatase function through an inhibitory wedge. Science 279, 88–91 (1998). [PubMed: 9417031]
26. Xu Z, Weiss A, Negative regulation of CD45 by differential homodimerization of the alternatively spliced isoforms. Nat Immunol 3, 764–771 (2002). [PubMed: 12134145]
27. Nam HJ, Poy F, Krueger NX, Saito H, Frederick CA, Crystal structure of the tandem phosphatase domains of RPTP LAR. Cell 97, 449–457 (1999). [PubMed: 10338209]
28. Nam HJ, Poy F, Saito H, Frederick CA, Structural basis for the function and regulation of the receptor protein tyrosine phosphatase CD45. J Exp Med 201, 441–452 (2005). [PubMed: 15684325]
29. Almo SC et al. , Structural genomics of protein phosphatases. J Struct Funct Genomics 8, 121–140 (2007). [PubMed: 18058037]
30. Barr AJ et al. , Large-scale structural analysis of the classical human protein tyrosine phosphatome. Cell 136, 352–363 (2009). [PubMed: 19167335]

31. Hermiston ML et al. , Differential impact of the CD45 juxtamembrane wedge on central and peripheral T cell receptor responses. Proc Natl Acad Sci U S A 106, 546–551 (2009). [PubMed: 19129486]
32. Fujikawa A et al. , A head-to-toe dimerization has physiological relevance for ligand-induced inactivation of protein tyrosine receptor type Z. J Biol Chem 294, 14953–14965 (2019).
33. Tertoolen LG et al. , Dimerization of receptor protein-tyrosine phosphatase alpha in living cells. BMC Cell Biol 2, 8 (2001). [PubMed: 11401727]
34. Fan Z et al. , High-Affinity Bent beta2-Integrin Molecules in Arresting Neutrophils Face Each Other through Binding to ICAMs In cis. Cell Rep 26, 119–130 e115 (2019).
35. Harris LJ, Larson SB, Hasel KW, McPherson A, Refined structure of an intact IgG2a monoclonal antibody. Biochemistry 36, 1581–1597 (1997). [PubMed: 9048542]
36. Sonnenburg ED, Bilwes A, Hunter T, Noel JP, The structure of the membrane distal phosphatase domain of RPTPalpha reveals interdomain flexibility and an SH2 domain interaction region. Biochemistry 42, 7904–7914 (2003). [PubMed: 12834342]
37. Cowan-Jacob SW et al. , The crystal structure of a c-Src complex in an active conformation suggests possible steps in c-Src activation. Structure 13, 861–871 (2005). [PubMed: 15939018]
38. Spassov DS, Ruiz-Saenz A, Piple A, Moasser MM, A Dimerization Function in the Intrinsically Disordered N-Terminal Region of Src. Cell Rep 25, 449–463 e444 (2018).
39. Shrestha D, Jenei A, Nagy P, Vereb G, Szollosi J, Understanding FRET as a research tool for cellular studies. Int J Mol Sci 16, 6718–6756 (2015). [PubMed: 25815593]
40. Del Pozo MA et al. , Integrins regulate GTP-Rac localized effector interactions through dissociation of Rho-GDI. Nat Cell Biol 4, 232–239 (2002). [PubMed: 11862216]
41. Tzima E et al. , Activation of Rac1 by shear stress in endothelial cells mediates both cytoskeletal reorganization and effects on gene expression. EMBO J 21, 6791–6800 (2002). [PubMed: 12486000]
42. Chen Y, Mauldin JP, Day RN, Periasamy A, Characterization of spectral FRET imaging microscopy for monitoring nuclear protein interactions. J Microsc 228, 139–152 (2007). [PubMed: 17970914]
43. Periasamy A, Wallrabe H, Chen Y, Barroso M, Chapter 22: Quantitation of protein-protein interactions: confocal FRET microscopy. Methods Cell Biol 89, 569–598 (2008). [PubMed: 19118691]
44. Sun Y, Rombola C, Jyothikumar V, Periasamy A, Forster resonance energy transfer microscopy and spectroscopy for localizing protein-protein interactions in living cells. Cytometry A 83, 780–793 (2013). [PubMed: 23813736]
45. Bastiaens PI, Jovin TM, Microspectroscopic imaging tracks the intracellular processing of a signal transduction protein: fluorescent-labeled protein kinase C beta I. Proc Natl Acad Sci U S A 93, 8407–8412 (1996). [PubMed: 8710884]
46. Zal T, Gascoigne NR, Photobleaching-corrected FRET efficiency imaging of live cells. Biophys J 86, 3923–3939 (2004). [PubMed: 15189889]
47. Digman MA, Caiolfa VR, Zamai M, Gratton E, The phasor approach to fluorescence lifetime imaging analysis. Biophys J 94, L14–16 (2008). [PubMed: 17981902]
48. Day RN, Measuring protein interactions using Forster resonance energy transfer and fluorescence lifetime imaging microscopy. Methods 66, 200–207 (2014). [PubMed: 23806643]
49. Ranjit S, Malacrida L, Jameson DM, Gratton E, Fit-free analysis of fluorescence lifetime imaging data using the phasor approach. Nat Protoc 13, 1979–2004 (2018). [PubMed: 30190551]
50. Tehrani S, Tomasevic N, Weed S, Sakowicz R, Cooper JA, Src phosphorylation of cortactin enhances actin assembly. Proc Natl Acad Sci U S A 104, 11933–11938 (2007).
51. He Y et al. , Src and cortactin promote lamellipodia protrusion and filopodia formation and stability in growth cones. Mol Biol Cell 26, 3229–3244 (2015). [PubMed: 26224308]
52. Truffi M et al. , RPTPalpha controls epithelial adherens junctions, linking E-cadherin engagement to c-Src-mediated phosphorylation of cortactin. J Cell Sci 127, 2420–2432 (2014). [PubMed: 24652832]

53. Cheng SY, Sun G, Schlaepfer DD, Pallen CJ, Grb2 promotes integrin-induced focal adhesion kinase (FAK) autophosphorylation and directs the phosphorylation of protein tyrosine phosphatase alpha by the Src-FAK kinase complex. Mol Cell Biol 34, 348–361 (2014). [PubMed: 24248601]
54. Su J, Muranjan M, Sap J, Receptor protein tyrosine phosphatase alpha activates Src-family kinases and controls integrin-mediated responses in fibroblasts. Curr Biol 9, 505–511 (1999). [PubMed: 10339427]
55. Doody KM et al. , Targeting phosphatase-dependent proteoglycan switch for rheumatoid arthritis therapy. Sci Transl Med 7, 288ra276 (2015).
56. Xie Y et al. , Protein-tyrosine phosphatase (PTP) wedge domain peptides: a novel approach for inhibition of PTP function and augmentation of protein-tyrosine kinase function. J Biol Chem 281, 16482–16492 (2006).
57. Matozo HC et al. , Low-resolution structure and fluorescence anisotropy analysis of protein tyrosine phosphatase eta catalytic domain. Biophys J 92, 4424–4432 (2007). [PubMed: 17400699]
58. Ran H, Tsutsumi R, Araki T, Neel BG, Sticking It to Cancer with Molecular Glue for SHP2. Cancer Cell 30, 194–196 (2016). [PubMed: 27505669]
59. Krishnan N, Konidaris KF, Gasser G, Tonks NK, A potent, selective, and orally bioavailable inhibitor of the protein-tyrosine phosphatase PTP1B improves insulin and leptin signaling in animal models. J Biol Chem 293, 1517–1525 (2018). [PubMed: 29217773]
60. Zhang Y et al. , PTPsigma inhibitors promote hematopoietic stem cell regeneration. Nat Commun 10, 3667 (2019). [PubMed: 31413255]
61. Bottini N, Firestein GS, Duality of fibroblast-like synoviocytes in RA: passive responders and imprinted aggressors. Nat Rev Rheumatol 9, 24–33 (2013). [PubMed: 23147896]
62. Svensson MND et al. , Synoviocyte-targeted therapy synergizes with TNF inhibition in arthritis reversal. Sci Adv 6, eaba4353 (2020).
63. Yao Z, Stagljar I, Multiple functions of protein phosphatases in receptor tyrosine kinase signaling revealed by interactome analysis. Mol Cell Oncol 4, e1297101 (2017).
64. den Hertog J, Tracy S, Hunter T, Phosphorylation of receptor protein-tyrosine phosphatase alpha on Tyr789, a binding site for the SH3-SH2-SH3 adaptor protein GRB-2 in vivo. EMBO J 13, 3020–3032 (1994). [PubMed: 7518772]
65. Vacaru AM, den Hertog J, Catalytically active membrane-distal phosphatase domain of receptor protein-tyrosine phosphatase alpha is required for Src activation. FEBS J 277, 1562–1570 (2010). [PubMed: 20158519]
66. Cohen-Sharir Y et al. , Protein tyrosine phosphatase alpha inhibits hypothalamic leptin receptor signaling and regulates body weight in vivo. FASEB J 33, 5101–5111 (2019). [PubMed: 30615487]
67. Guma M et al. , Caspase 1-independent activation of interleukin-1beta in neutrophil-predominant inflammation. Arthritis Rheum 60, 3642–3650 (2009). [PubMed: 19950258]
68. Emsley P, Lohkamp B, Scott WG, Cowtan K, Features and development of Coot. Acta Crystallogr D Biol Crystallogr 66, 486–501 (2010). [PubMed: 20383002]
69. Johnson JL, Pestonjamasp K, Kiosses WB, Catz SD, Super-Resolution Microscopy and Particle-Tracking Approaches for the Study of Vesicular Trafficking in Primary Neutrophils. Methods Mol Biol 2233, 193–202 (2021). [PubMed: 33222136]
70. Marki A et al. , Elongated neutrophil-derived structures are blood-borne microparticles formed by rolling neutrophils during sepsis. J Exp Med 218, (2021).
71. Abercrombie M, Heaysman JE, Pegrum SM, The locomotion of fibroblasts in culture. IV. Electron microscopy of the leading lamella. Exp Cell Res 67, 359–367 (1971). [PubMed: 5097522]
72. Abraham VC, Krishnamurthi V, Taylor DL, Lanni F, The actin-based nanomachine at the leading edge of migrating cells. Biophys J 77, 1721–1732 (1999). [PubMed: 10465781]
73. Atilgan E, Wirtz D, Sun SX, Morphology of the lamellipodium and organization of actin filaments at the leading edge of crawling cells. Biophys J 89, 3589–3602 (2005). [PubMed: 16085776]
74. Kraynov VS et al. , Localized Rac activation dynamics visualized in living cells. Science 290, 333–337 (2000). [PubMed: 11030651]

75. Chamberlain CE, Kraynov VS, Hahn KM, Imaging spatiotemporal dynamics of Rac activation in vivo with FLAIR. Methods Enzymol 325, 389–400 (2000). [PubMed: 11036621]

76. Elangovan M et al. , Characterization of one- and two-photon excitation fluorescence resonance energy transfer microscopy. Methods 29, 58–73 (2003). [PubMed: 12543072]

77. Wouters FS, Bastiaens PI, Wirtz KW, Jovin TM, FRET microscopy demonstrates molecular association of non-specific lipid transfer protein (nsL-TP) with fatty acid oxidation enzymes in peroxisomes. EMBO J 17, 7179–7189 (1998). [PubMed: 9857175]

78. Day RN, Periasamy A, Schaufele F, Fluorescence resonance energy transfer microscopy of localized protein interactions in the living cell nucleus. Methods 25, 4–18 (2001). [PubMed: 11558993]

79. Carlon-Andres I, Padilla-Parra S, Quantitative FRET-FLIM-BlaM to Assess the Extent of HIV-1 Fusion in Live Cells. Viruses 12, (2020).

80. Coomer CAet al. , Single-cell glycolytic activity regulates membrane tension and HIV-1 fusion. PLoS Pathog 16, e1008359 (2020).

81. Sun Y, Day RN, Periasamy A, Investigating protein-protein interactions in living cells using fluorescence lifetime imaging microscopy. Nat Protoc 6, 1324–1340 (2011). [PubMed: 21886099]

82. Benkahla MA et al. , HLA class I hyper-expression unmasks beta cells but not alpha cells to the immune system in pre-diabetes. J Autoimmun 119, 102628 (2021).

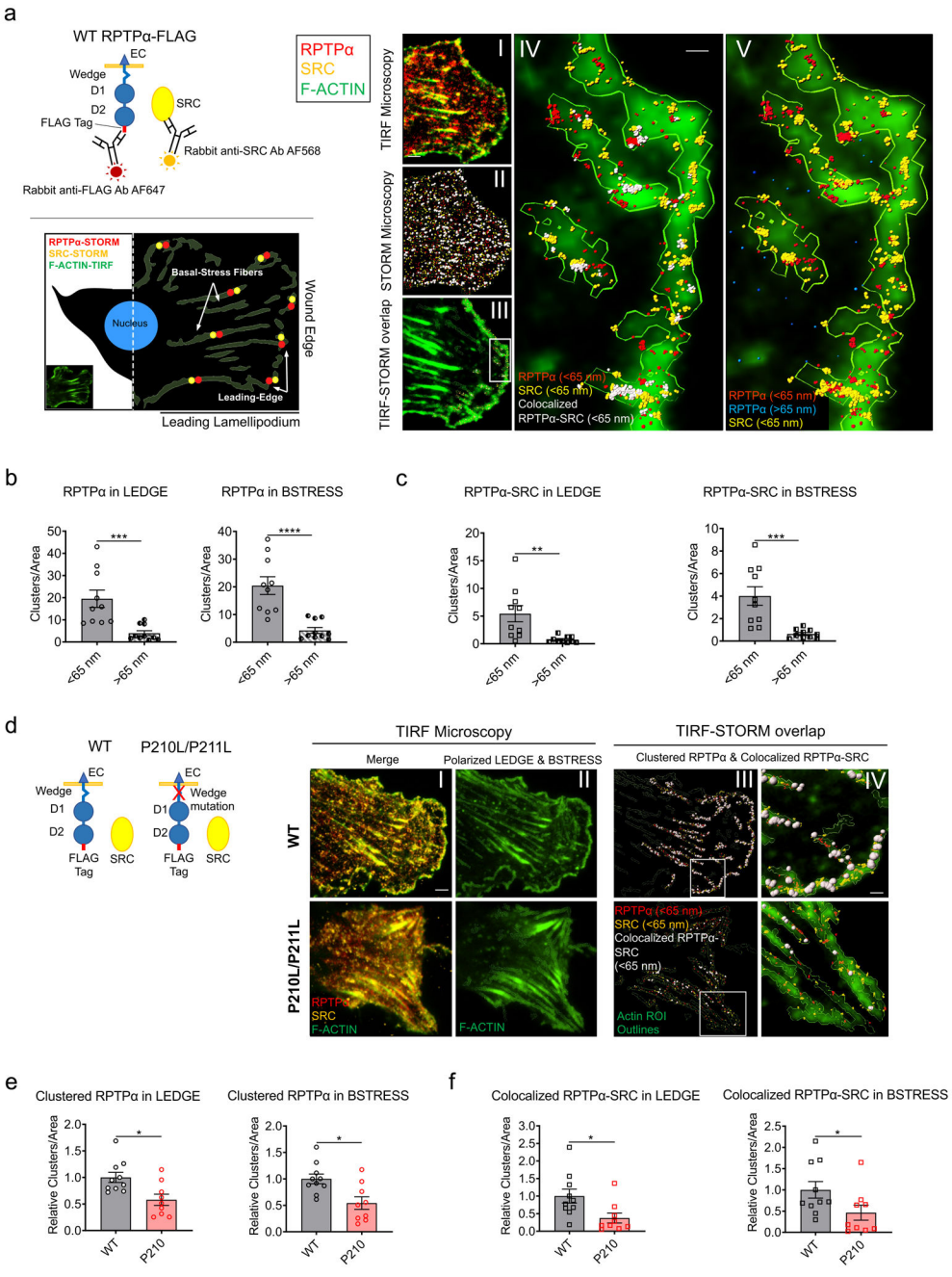

Figure 1. Super-resolution microscopy of migrating SF suggests that RPTPα clusters interact with SRC along actin stress fibers

(**a**) Left side: drawn schematic of our experimental targets and reagents labelling strategy (upper left) and a diagram of cellular compartments for migrating cell with leading lamellipodium showing leading edge (LEDGE) and polarized basal stress fibers (BSTRESS, lower left). Right side: TIRF micrograph (**I**), STORM localization map (**II**), and low (**III**) vs high (**IV, V**) magnification of leading lamellipodial edge rendering of overlap TIRF-STORM images of WT RPTPα-expressing SF, with localization map of clustered (red spheres,

distance <65 nm) vs non clustered (blue spheres, distance >65 nm) RPTPα, clustered (yellow spheres, distance <65 nm) SRC, and colocalized RPTPα-SRC (white spheres, distance <65 nm) overlaid on the F-actin TIRF image (green). Scale bar in **I** and **IV** is 5 μm and 500 nm, respectively. (**b,c**) Density of clustered vs non clustered RPTPα (**b**) or colocalized vs non colocalized RPTPα-SRC (**c**) in LEDGE (left) or BSTRESS (right) of WT RPTPα-expressing SF. (**d**) Left side: drawn schematic of our experimental targets, reagents and labelling strategy. Right side: representative TIRF (**I, II**) and low (**III**) vs high (**IV**) magnification overlap TIRF-STORM images of SF expressing WT RPTPα-FLAG (WT, upper panels) compared with SF expressing P210L/P211L RPTPα-FLAG (P210, lower panels) with localization map coded as in **a-III,IV**. Scale bar in **I** and **IV** is 3 μm and 1 μm, respectively. Relative density of clustered RPTPα (**e**) or colocalized RPTPα-SRC (**f**) in LEDGE and BSTRESS of WT and P210 cells. (**b,c,e,f**) Each point represents a transfected cell. N=10 cells per construct across 4 experiments using 4 αKO lines for WT, N=9 cells per construct across 3 experiments using 3 αKO lines for P210. Data are means±SEM. **** p ≤0.0001, *** p ≤0.001, ** p ≤0.01, * p ≤0.05 by Mann-Whitney.

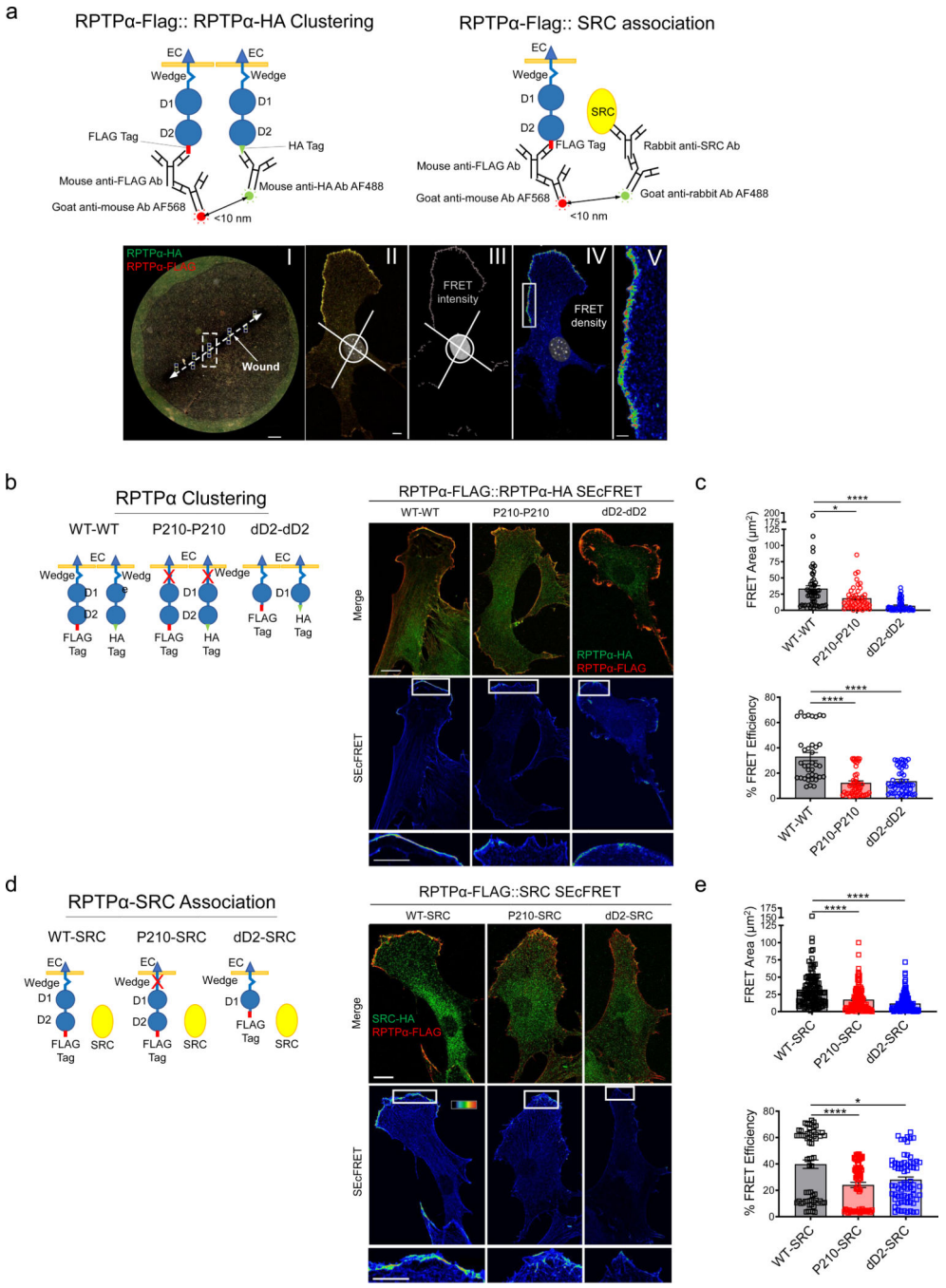

Figure 2. SEcFRET-assessment of migrating SF suggests that clustering of RPTPα correlates with association with SRC

(**a**) Upper part: drawn schematic of our experimental targets and reagents labelling strategy. Lower part: (**I**) low resolution 10x multi-tiled stitched representative scratch wound in a monolayer of SF labeled with anti-FLAG-AF568 (red), anti-HA-AF488 (green), and Hoechst (blue) for SEcFRET analysis of migrating SF LEDGEs (scale bar is 1 mm); (**II-V**), method for analyzing FRET-positive regions: each cell is quadri-sected (**II**, color code is as in **I**, scale bar is 5 μm), FRET zones auto-outlined (**III**); (**IV**) SEcFRET density map image,

magnified in **V** (scale bar is 500 nm). (**b**) Left side: drawn schematic of our experimental targets and reagents labelling strategy. Right side: representative FLAG- and HA-RPTPα staining (upper panels, scale bar is 10 μm) and LEDGE SEcFRET localization in WT-WT, P210-P210 and dD2-dD2 SF (middle panels) and highlighted in magnified box insets (lower panels, scale bar is 2 μm). (**c**) SEcFRET signal (upper graph) and calculated % FRET efficiency (lower graph) of RPTPα homodimer in the 90-degree quadrant corresponding to the LEDGE. (**d**) Left side: schematic of our experimental targets, reagents labelling strategy. Right side: representative RPTPα-FLAG and SRC staining (upper panels, scale bar is 10 μm) and LEDGE SEcFRET localization in WT-SRC, P210-SRC and dD2-SRC SF (middle panels) and highlighted in magnified box insets (lower panels, scale bar is 2 μm). (**e**) SEcFRET signal (upper graph) and calculated % FRET efficiency (lower graph) of RPTPα-SRC association in the 90-degree quadrant corresponding to the LEDGE. Each point in (**c,e**) represents a transfected cell. N= 40–60 cells per construct across 2 experiments using 2 αKO lines for RPTPα homodimer, N= 65–130 cells per construct across 3 experiments using 3 αKO lines for RPTPα-SRC association. Data are means±SEM. **** $p \leq 0.0001$, * $p \leq 0.05$ by Kluskal-Wallis with corrected Dunn's test.

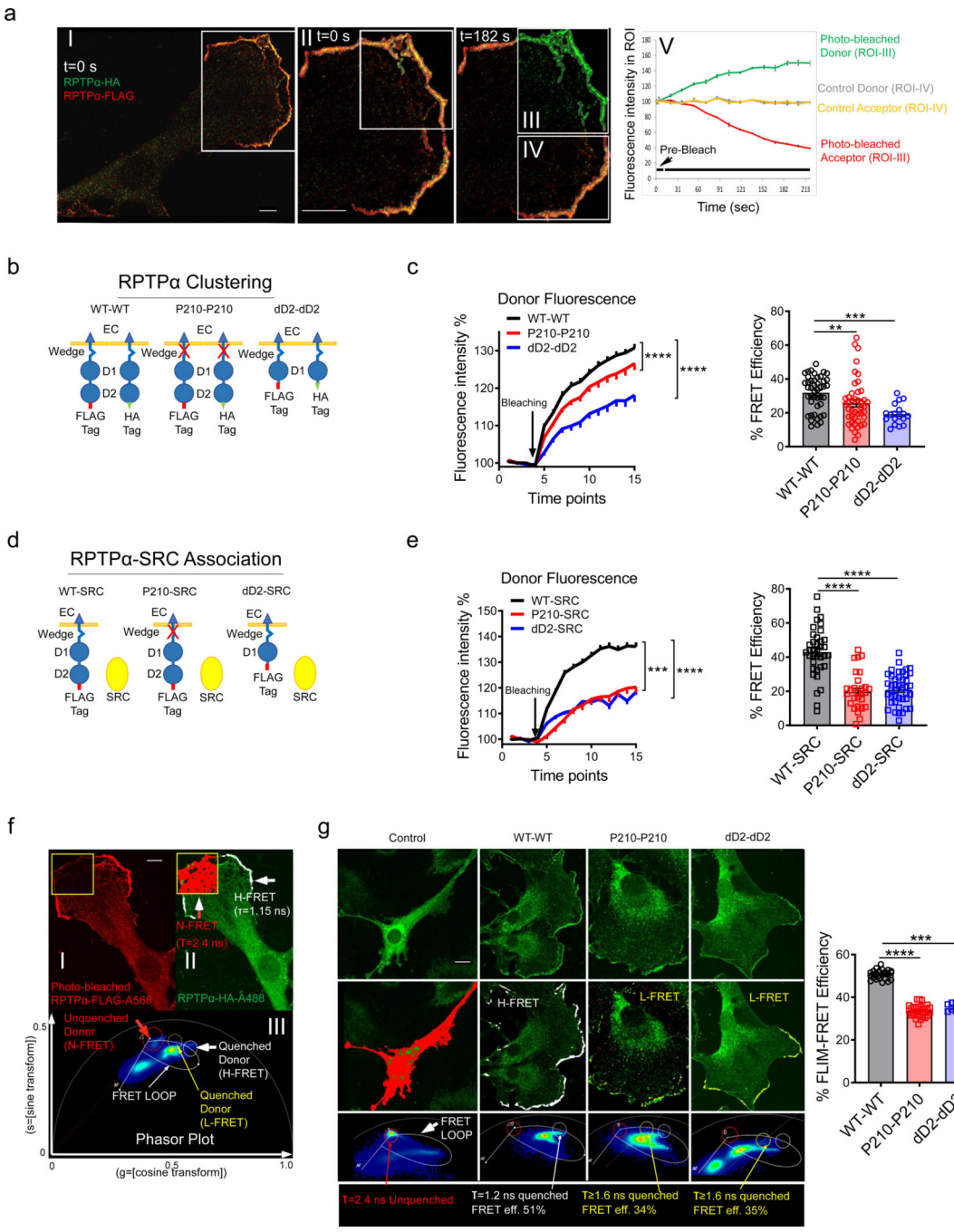

Figure 3. ApFRET and FLIM assessment of migrating SF suggests that clustering of RPTPα correlates with association with SRC

(**a**) Typical apFRET images. The whole cell (box in **I**) was imaged at t=0 with donor and acceptor merged (**I**, scale bar is 5 μm), then magnified in **II** (scale bar is 5 μm) to highlight bleached ROI (box in **II**) and then post bleached at t=182 sec - showing bleached (**III**) and unbleached (**IV**) portions of the lamellipodium. **V** shows representative post-photo-bleaching apFRET analysis: the relative fluorescence vs time graphs of photo-bleached anti-FLAG-AF568 acceptor (red) and unquenched anti-HA-AF488 donor (green) are shown for

photo-bleached ROIs from III, together with graphs for donor (black) and acceptor (yellow) for control non bleached ROI from IV. (**b, d**) Summary of experimental setting for panel **c** and **e**. (**c**, **e**) Post-bleaching fluorescence intensity (left graph) and % FRET efficiency (right graph) of donor in apFRET of RPTPα clustering in WT-WT, P210-P210 and dD2-dD2 SF (**c**) and of RPTPα-SRC association in WT-SRC, P210-SRC and dD2-SRC SF (**e**). Each point in (**c**,**e**) represents a ROI which stringently outlines the cell lamellipodium. N= 7–11 cells for (**c**) and N=9–14 cells for (**e**) per construct across 2 experiments using 2 αKO lines. (**f**) Representative Fast Lifetime Contrast (FALCON) FLIM acquisition and phasor plot analysis of RPTPα clustering. (**I**) Post-bleached acceptor signal (bleached area in yellow box ROI); (**II**) FLIM acquired image highlighting the donor unquenching in bleached area (N-FRET, red pseudocolor in yellow box ROI) contrasting with the highly quenched (>50% efficiency) FRET (H-FRET) positive regions in white; (**III**) location of N-FRET (red circle) vs H-FRET (white circle) vs <35% FRET efficiency (L-FRET) pixels in the phasor loop. Scale bar is 10 μm. (**g**) Representative FLIM images of RPTPα clustering in WT-WT, P210-P210 and dD2-dD2 SF (left panel, scale bar is 10 μm) and quantification of % FLIM-FRET efficiency (right panel). Fluorescent Images in upper panels are RPTPα donor fluorescent signal. Middle panels are FLIM images displaying H-FRET vs L-FRET pseudocolored in white and yellow respectively. Lifetimes are shown in lower panels. Donor only control lifetimes cluster in red circles in Phasor loops. Each point represents a transfected cell. N= 10–33 cells per construct across 2 experiments using 2 αKO lines. Data are means±SEM. **** $p \leq 0.0001$, *** $p \leq 0.001$, ** $p \leq 0.01$, by Kluskal-Wallis with corrected Dunn's test for (**c**) and (**e**) right panels, or ordinary one-way ANOVA calculated on AUC (Dunnett's multiple comparison test) for (**c**) and (**e**), left panels.

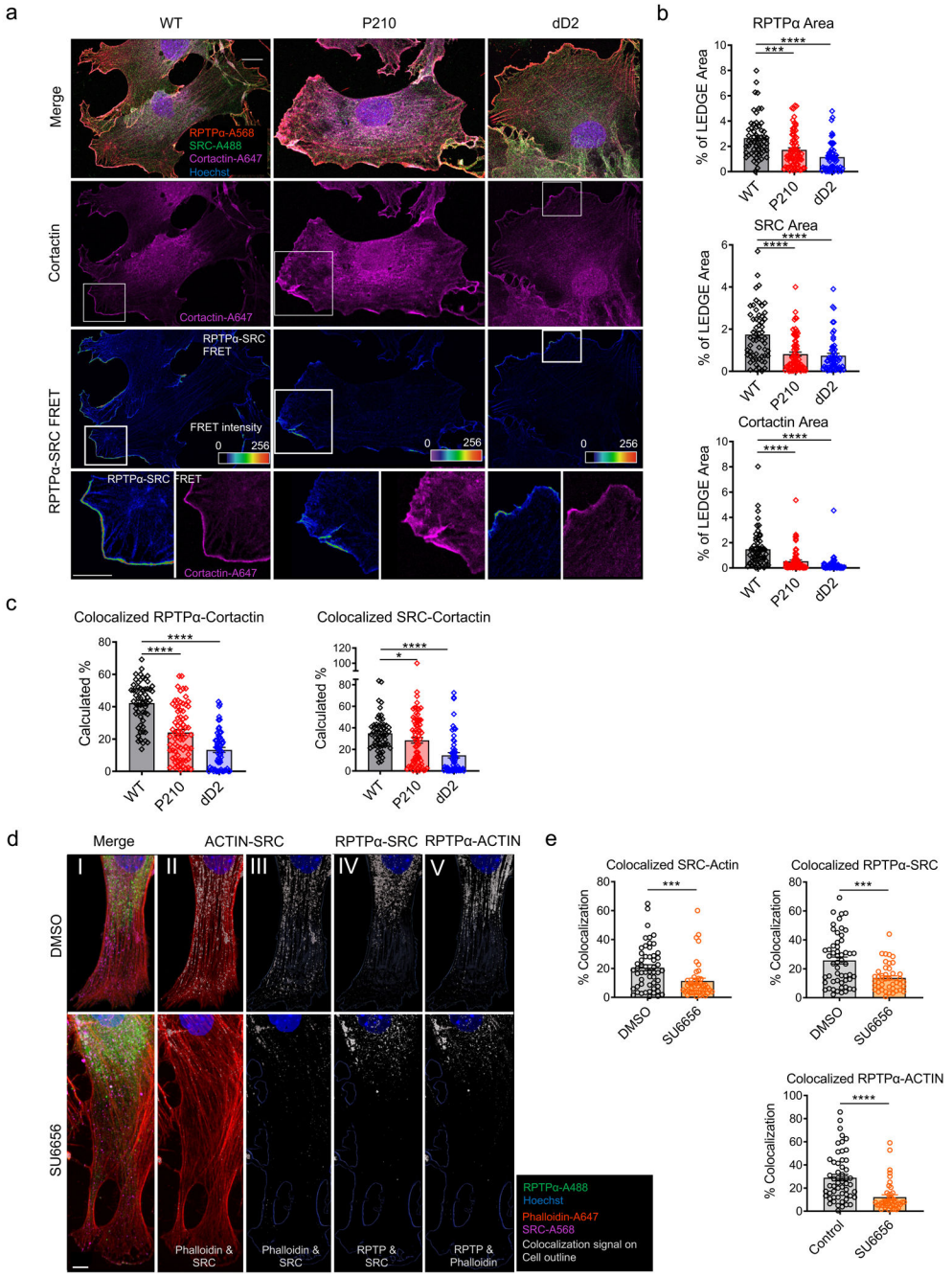

Figure 4. RPTPα clustering correlates with cortactin recruitment to the LEDGE of migrating SF and its co-localization with RPTPα and SRC

(**a**) Representative images of wound edge migrating SF transfected with WT PTPRA-FLAG (WT), P210L/P211L PTPRA-FLAG (P210) or dD2 PTPRA-FLAG (dD2) expression constructs. Upper panel: staining with anti-FLAG-AF568 (red), anti-SRC-AF488 (green), anti-cortactin-AF647 (magenta) and Hoechst (blue) (scale bar is 10 μm). The second from top panels display cortactin only (magenta). The third from top and the bottom panels show the SEcFRET images of these representative cells, and a zoomed-in panel series

(scale bar is 10 μm). (**b**) Quantification of RPTPα, SRC and cortactin positive area in the LEDGE of transfected migrating SF. (**c**) Quantification of colocalized RPTPα-cortactin and SRC-cortactin in the LEDGE of transfected migrating SF. Each point in (**b,c**) represents a transfected cell. N= 5 αKO lines across 5 experiments. (**d**) Representative images of migrating αKO SF transfected with WT PTPRA-HA (WT) expression constructs treated with DMSO (control, upper panel) or SU6656 (SRC inhibitor, bottom panel) (scale bar is 10 μm). (**I)**: staining with anti-HA-AF488 (green), anti-SRC-AF568 (magenta), Phalloidin-AF647 (red) and hoechst (blue). (**II,III)**: SRC-F-ACTIN colocalization signal (gray) on cell outline with (**II**) or without (**III**) phalloidin (red). (**IV)**: RPTPα-SRC and (**V)**: SRC-F-ACTIN colocalization signal (gray) on cell outline. (**e**) Quantification of colocalized SRC-F-ACTIN (left), RPTPα-SRC (upper right) and RPTPα -F-ACTIN (lower right) in transfected migrating SF. Each point represents a transfected cell. N=43–54 cells per group across 2 experiments using 2 αKO lines. Data are means±SEM. **** $p \leq 0.0001$, *** $p \leq 0.001$, by Kluskal-Wallis with corrected Dunn's test (panels **b, c**) or Mann-Whitney (panel **e**)).

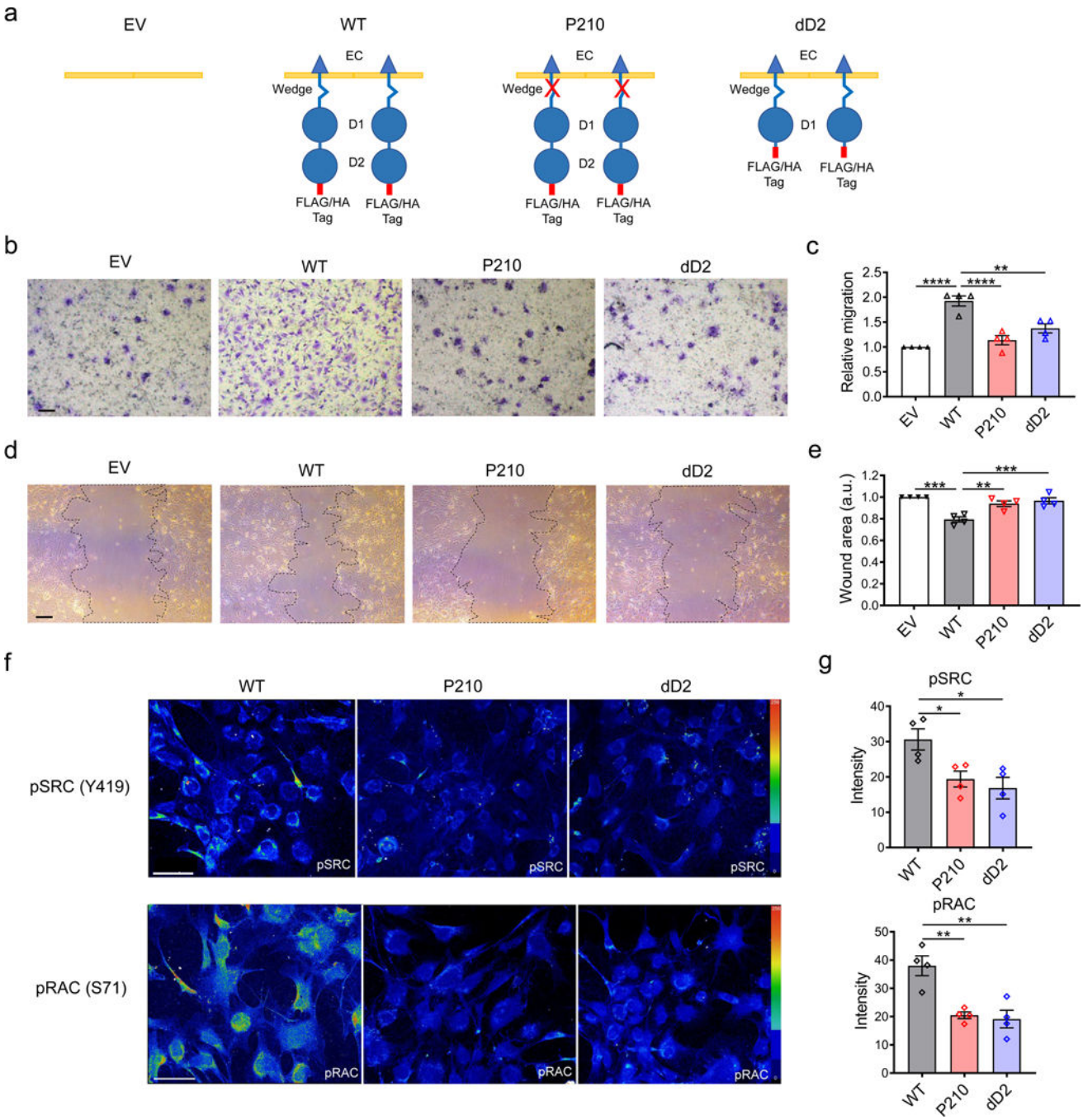

Figure 5. Clustering-impaired RPTPα mutations impair SF migration and phosphorylation of SRC and RAC

(**a**) Summary of experimental setting for the experiment outlined in **b**-**g**. Representative images (**b**) and migration rate (**c**) of EV, WT, P210 or dD2 SF, normalized by EV. Representative images of scratched wound (**d**) and wound area reduction (**e**) in monolayers of EV, WT, P210 or dD2 SF. Graph shows ratio between the area at 24h vs time 0 normalized by the area change of EV. Scale bar in (**b**,**d**) is 200 μm. Each point (c,e) represents a different transfected cell line (N=4) across 4 experiments. Representative heat

maps (**f**), with scale bar (100μm) and mean fluorescence intensity (**g**) of images of pSRC (Tyr^{419}), pRAC (Ser^{71}) in monolayers of migrating WT, P210 or dD2 SF. Each point represents the intensity level in a selected microscopy field. N=4 fields per construct across 2 experiments using 2 αKO lines. Data are means±SEM. **** $p \leq 0.0001$, *** $p \leq 0.001$, ** $p \leq 0.01$, * $p \leq 0.05$ by ordinary one-way ANOVA (Dunnett's multiple comparison test).

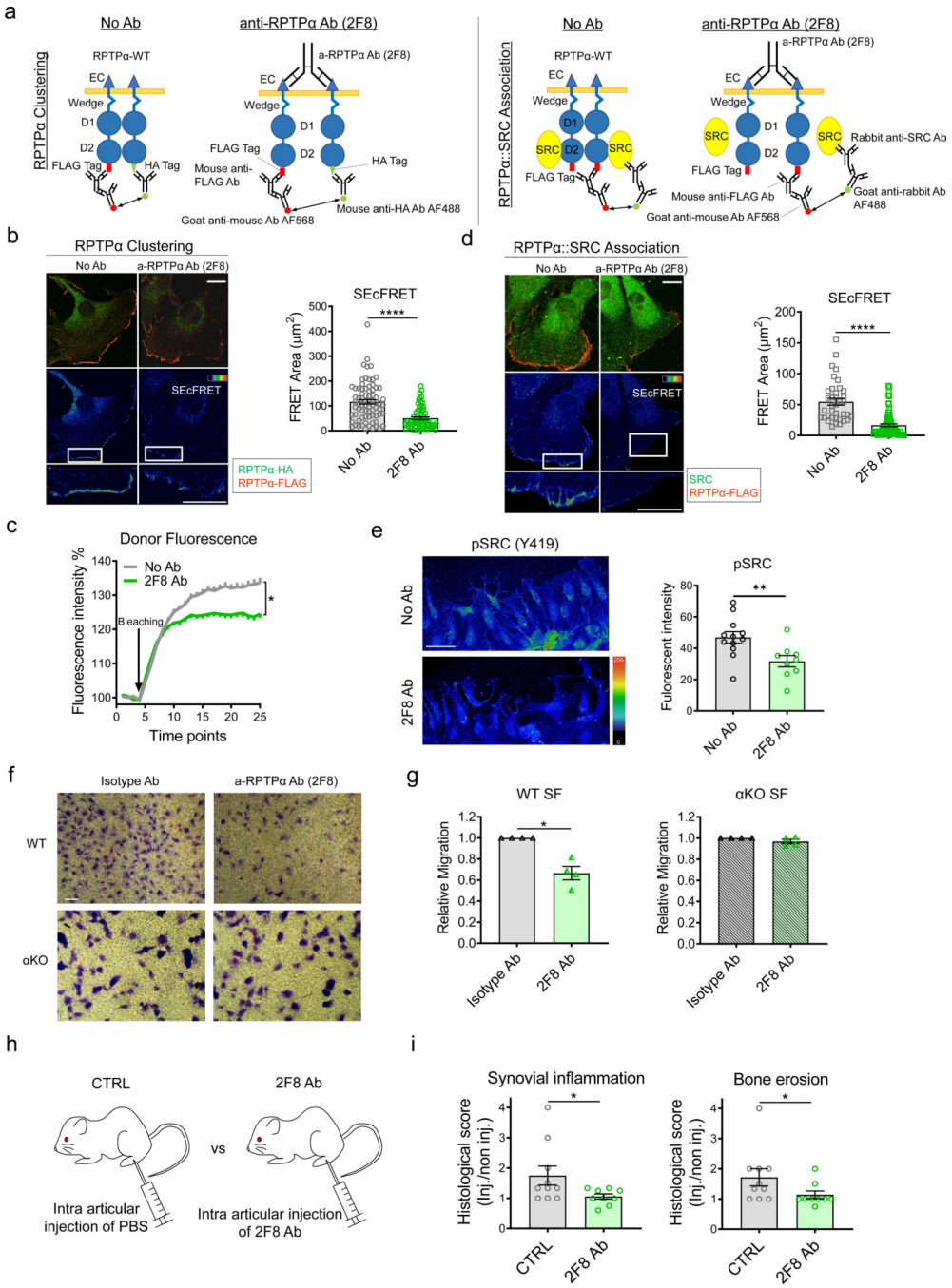

Figure 6. RPTPα-blocking Ab reduces RPTPα clustering and association with SRC at the LEDGE of migrating SF

(**a**) Drawn schematic of our experimental targets and reagents labelling strategy for the experiment outlined in **b-d**. SF were transfected with WT PTPRA-FLAG with (panels **b,c**, WT-WT) or without (panel **d**, WT-SRC) WT PTPRA-HA and incubated with isotype Ab or anti-RPTPα blocking Ab (2F8). (**b,d**) Left: representative SEcFRET image (scale bar is 20 μm). Right: quantified total SEcFRET signal areas at the LEDGE. Each point represents a transfected cell. N=65–76 cells for **b**, N=37–75 cells for **d** across 3 experiments using

3 αKO lines. (**c**) Post-bleaching time resolved average fluorescence intensity profile of dequenched donor signal of RPTPα clustering using the apFRET method. N=12–13 cells per group across 2 experiments using 2 αKO lines. (**e**) Representative heat maps (left) and mean fluorescence intensity (right) of images of pSRC (Tyr^{419}) in monolayers of WT SF incubated with or without anti-RPTPα blocking Ab (2F8). Scale bar is 100 μm. Each point represents the intensity level in a microscopy field. N=9–12 fields and 2 cell lines across 2 experiments. (**f,g**) Representative images (**f**) and migration rate (**g**) of WT (N=4 lines) or αKO (N=4 lines) SF, normalized by migration of SF incubated with isotype control Ab. Scale bar in (**f**) is 200 μm. Each point represents a different cell line across 4 experiments. (**h,i**) Schematic of experiment (**h**) and histological scores (**i**, Left: synovial inflammation, Right: bone erosion) for STIA in female BALB/c mice subjected to injection with anti-RPTPα blocking Ab (2F8) or PBS (2F8 Ab: N= 9, PBS: N= 10). Each point represents the score ratio of 2F8Ab or saline injected joint vs contralateral non-injected joint of a mouse. Graphs in **e**, **g** and **i** show means and SEM. **** $p \leq 0.0001$, ** $p \leq 0.01$, * $p \leq 0.05$ by Mann-Whitney (panel **b**,**d,e,i)**, unpaired t-test calculated on AUC (panel **c**) or paired t test (panel **g**).

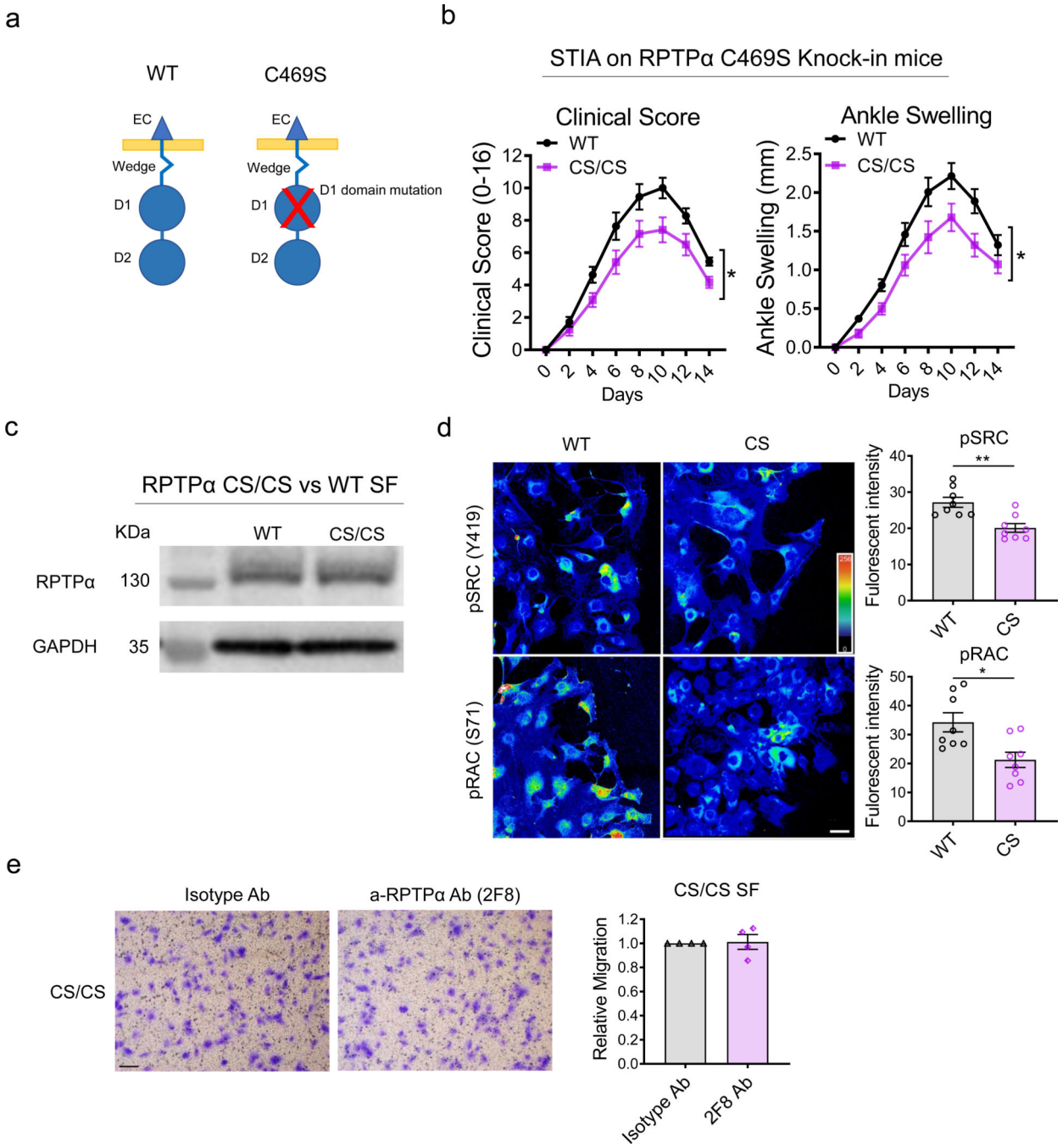

Figure 7. RPTPα inactivation reduced arthritis severity in mice and removes the inhibitory effect of 2F8 on ex vivo SF migration

(**a**) Drawn schematic for the experiments in **b-e**. (**b**) Clinical score (left) and ankle thickness (right) for STIA in female WT (N=11) and homozygous RPTPα C469S (CS/CS, N=12) littermate mice. (**c**) RPTPα vs GAPDH expression in lysates of SF derived from WT or CS/CS mice. Data is representative n=2 independent experiments. (**d**) Representative heat maps (left) and mean fluorescence intensity (right) of images of pSRC (Tyr^{419}) and pRAC (Ser^{71}) in monolayers of WT, CS/CS SF. Each point represents intensity level in a selected

field. N=3 WT and 3 CS lines across 3 experiments (**e**) Representative images (left) and migration rate of CS/CS SF (N=4 lines) (right), incubated with 2F8 Ab or isotype control Ab, normalized by isotype control Ab. Scale bar is 200 μm. Each point represents a different SF line across 4 experiments. Data are means±SEM. ** $p \leq 0.01$, * $p \leq 0.05$ by unpaired t-test calculated on AUC (panel **b**), Mann-Whitney (panel **d)** or paired t test (panel **e**).

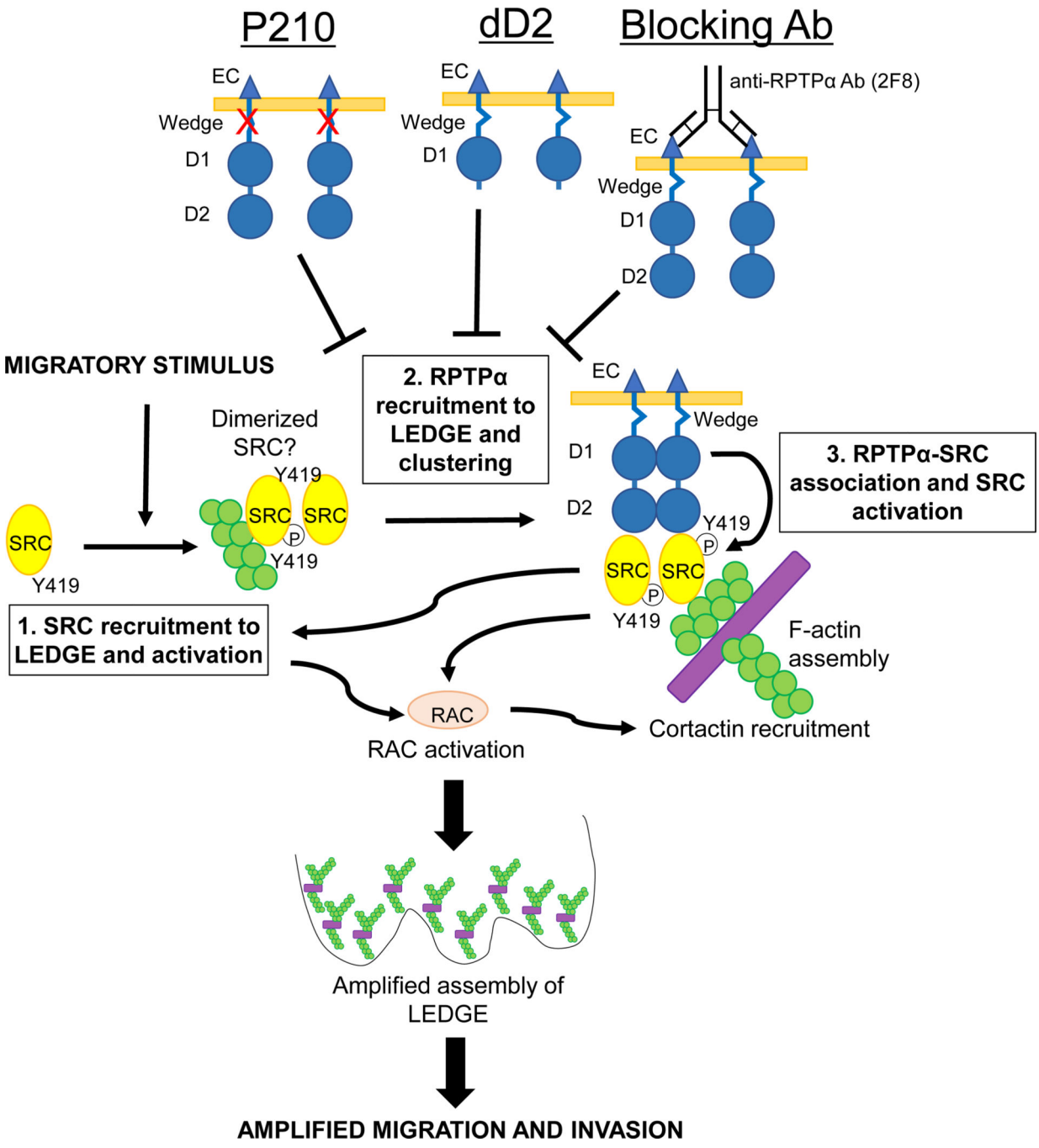

Figure 8. Working model for relationship between clustering of RPTPα and SRC activation at the LEDGE of migrating SF

Drawn schematic of our proposal working model. Activation of SRC induces LEDGE formation also through downstream Rac activation and promotes recruitment and clustering of RPTPα at the LEDGE which in turn amplifies SRC activation and LEDGE assembly. De-clustering RPTPα mutations (P210, dD2) or Ab (2F8) impair RPTPα recruitment and clustering at the LEDGE and impair this amplification mechanism.